Geophysical Journal International

Geophys. J. Int. (2014) **198,** 90–109
Advance Access publication 2014 April 29
GJI Seismology

doi: 10.1093/gji/ggu115

Single-station cross-correlation analysis of ambient seismic noise: application to stations in the surroundings of the 2008 Iwate-Miyagi Nairiku earthquake

Manuel Hobiger,[1,*] Ulrich Wegler,[1] Katsuhiko Shiomi[2] and Hisashi Nakahara[3]

[1] *Federal Institute for Geosciences and Natural Resources (BGR), Hanover, Germany. E-mail: manuel.hobiger@sed.ethz.ch*
[2] *National Research Institute for Earth Science and Disaster Prevention (NIED), Tsukuba, Japan*
[3] *Department of Geophysics, Graduate School of Science, Tohoku University, Sendai, Japan*

Accepted 2014 March 24. Received 2014 February 14; in original form 2013 September 24

SUMMARY

We introduce the single-station cross-correlation (SC) technique of processing ambient seismic noise and compare its results with the established cross-correlation (CC) and autocorrelation (AC) techniques. While CC is the correlation of the signals of two seismic stations with each other and AC is the correlation of a signal with itself, SC is the correlation of two different components of a single three-component seismic sensor. The comparison of the three different correlation techniques shows that CCs give the best results at frequencies below 0.5 Hz and that SCs give the best results at higher frequencies. In all three processing techniques, ambient seismic noise is correlated in order to reconstruct the Green's function describing the wave propagation between the first and the second sensor. By relating the coda parts of the daily Green's functions with the long-term reference Green's functions, shear wave velocity changes are determined. Here, we apply this technique to the data of 20 seismic stations in the surroundings of the fault zone of the Iwate-Miyagi Nairiku earthquake ($M_W = 6.9$), which occurred on 2008 June 13, UTC (2008 June 14, Japan Standard Time) in the northern part of the Japanese island Honshu. The data range from 2008 January to 2011 June and therefore include the Tohoku earthquake ($M_W = 9.0$), which occurred on 2011 March 11, off the coast of northern Honshu. The data are analysed in five different frequency ranges between 0.125 and 4.0 Hz. The data show coseismic velocity changes for both earthquakes followed by a post-seismic velocity recovery. In general, the coseismic velocity changes increase with frequency. For the Iwate-Miyagi Nairiku earthquake, the strongest velocity changes occur close to the fault zone. Quickly recovering coseismic velocity changes can be separated from changes not recovering during the study period. For the Tohoku earthquake, the complete area is affected by coseismic velocity changes. A modelling of the depth of the coseismic velocity changes indicates that the Iwate-Miyagi Nairiku earthquake can be explained either by large shallow velocity changes or by small, but deep changes. For one station, the observations can only be explained by assuming deeper changes. For the Tohoku earthquake, the modelling shows that different parts of the study area are affected in different ways, some showing shallow changes, others deeper changes. Furthermore, seasonal velocity variations occur, which are compatible for the different stations above 0.5 Hz, with velocity maxima in autumn.

Key words: Interferometry; Surface waves and free oscillations; Coda waves; Wave scattering and diffraction.

1 INTRODUCTION

This study deals with the region around the Iwate-Miyagi Nairiku earthquake, which occurred on 2008 June 13 at 11:43 pm UTC (2008 June 14, 8:43 am local time). It took place in the northern part of Honshu island in Japan. Its moment magnitude was $M_W = 6.9$ and the hypocentre depth was about 5 km (NIED F-net 2008). The same area was also affected by the Tohoku earthquake, which occurred on 2011 March 11 at 05:46 am UTC (2011 March 11, 14:46 pm local time). This earthquake had a moment magnitude of $M_W = 9.0$ (Hirose *et al.* 2011). Its epicentre was about 190 km east of the

*Now at: Swiss Seismological Service (SED), ETH Zurich, Switzerland.

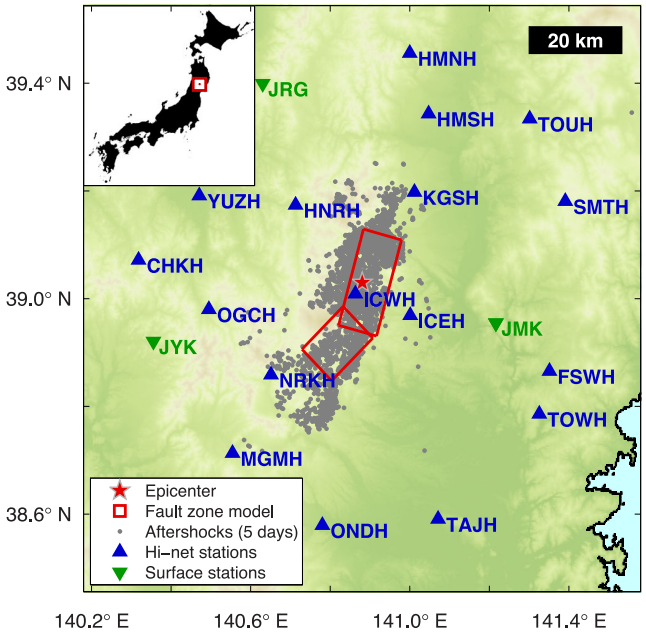

Figure 1. Map showing the locations of the 17 Hi-net stations and the three surface seismic stations with respect to the fault zone of the 2008 Iwate-Miyagi Nairiku earthquake. The grey dots indicate the aftershocks occurring in the 5 d following the earthquake. The two rectangles indicate the fault zone model of Ohta *et al.* (2008). The background topography is based on ASTER GDEM satellite data. The small inset shows the location of the study area in Japan.

Iwate-Miyagi Nairiku earthquake, but the fault zone stretched several hundred kilometres along the coast.

The rupture process of the Iwate-Miyagi Nairiku earthquake has been studied using strong motion records by Suzuki *et al.* (2010). They identified larger slips of over 6 m in the southern part of the fault zone. By analysing GPS measurements, Ohta *et al.* (2008) deduced a fault model consisting of two distinct fault planes, a northern one with a slip of 1.8 m and a southern one with a larger slip of 3.5 m. A surface KiK-net accelerometer station close to the epicentre (at the location of station ICWH; *cf.* Fig. 1) measured a vertical acceleration of 3.95 g (Aoi *et al.* 2008). Coseismic surface displacements of up to 1.2 m have been measured by InSAR (Takada *et al.* 2009) and major surface ruptures were also reported (Tsutsumi *et al.* 2010).

The Tohoku earthquake occurred off the coast of eastern Honshu, the fault zone had an area of roughly 500 km length along the coast and 200 km width (Hirose *et al.* 2011), but the largest slip was concentrated in a 300-km-long zone along the trench (Kubo & Kakehi 2013). A direct effect of the earthquake was also a large tsunami hitting the coast of Japan (Maeda *et al.* 2011). The earthquake induced seismic activity in many areas of Japan (Hirose *et al.* 2011). The largest of these earthquakes close to the study area of this paper was an *M*4.2 event on March 28 northwest of the study area (Okada *et al.* 2011). Addtionally, the Tohoku earthquake induced a large number of landslides in eastern Honshu (Wartman *et al.* 2011).

In a previous paper (Hobiger *et al.* 2012), we investigated coseismic and post-seismic velocity changes in the vicinity of the fault zone of the Iwate-Miyagi Nairiku earthquake using cross-correlation (CC) analysis. The CC analysis is based on the reconstruction of the Green's function for sensor pairs. The Green's function describes the wave propagation between two sensors. It corresponds to the seismometer record of the first sensor if an impulsive source was acting at the location of the second sensor. Using ultrasonic laboratory experiments, Lobkis & Weaver (2001) first showed that the Green's function can be reconstructed by correlating diffuse wave field data. This technique was transduced to seismology where Green's functions were reconstructed by using the diffuse part of the seismic coda (Campillo & Paul 2003; Paul *et al.* 2005) or by cross-correlating ambient seismic noise (Shapiro & Campillo 2004; Shapiro *et al.* 2005). The coda part of the Green's functions, which consists of scattered waves, can also be reconstructed by cross-correlating ambient noise (Sens-Schönfelder & Wegler 2006; Wegler & Sens-Schönfelder 2007). Many reviews on the noise correlation technique are available (Larose *et al.* 2006; Bensen *et al.* 2007; Wapenaar *et al.* 2010a,b; Sens-Schönfelder & Wegler 2011).

Recently, a considerable number of articles have reported changes of seismic wave velocities caused by earthquakes. Early observations of seismic velocity changes caused by earthquakes were performed by analysing the coda of earthquake doublets (Poupinet *et al.* 1984). With this technique, changes in velocity, source location and scattering properties can be distinguished (Snieder *et al.* 2002). Using repeating earthquakes, coseismic and post-seismic velocity changes have been measured for the 1999 İzmit and Düzce earthquakes (Peng & Ben-Zion 2006) and the 2003 Tokachi-Oki earthquake (Rubinstein *et al.* 2007).

Using artificial explosions as repeating events, coseismic or post-seismic velocity changes were measured for the 1992 Landers earthquake (Li *et al.* 1998), the 1999 Hector Mine earthquake (Li *et al.* 2003), volcanic activity and an *M*6.1 earthquake in Iwate prefecture (Nishimura *et al.* 2005) and the 2004 Parkfield earthquake (Li *et al.* 2006). Pre-seismic velocity changes were also reported for a drilling site in the Parkfield area (Niu *et al.* 2008).

In the last decade, there have also been a large number of studies measuring seismic velocity variations by correlating ambient seismic noise. Sens-Schönfelder & Wegler (2006) measured seasonal velocity variations at Merapi volcano using CC analysis and related them to groundwater level changes linked to precipitation variations. By auto- (AC) and cross-correlating seismic noise, Wegler & Sens-Schönfelder (2007) and Wegler *et al.* (2009) measured coseismic velocity drops for the 2004 Mid-Niigata earthquake. At Piton de la Fournaise volcano, seismic monitoring by cross-correlating seismic noise showed significant velocity decreases before eruptions (Brenguier *et al.* 2008b). Velocity changes caused by the 2007 Noto Hanto earthquake were measured using ACs (Ohmi *et al.* 2008). For the 2004 Parkfield earthquake, coseismic velocity drops (Brenguier *et al.* 2008a) and anisotropy changes (Durand *et al.* 2011) were reported. Also in the area of the 2008 Wenchuan earthquake, wave velocity changes were measured (Chen *et al.* 2010).

Another technique of detecting seismic velocity changes is by deconvolving the signals at the top and the bottom of a borehole. With this technique, velocity changes caused by the 2000 western Tottori earthquake (Sawazaki *et al.* 2009), the 2008 Iwate-Miyagi Nairiku earthquake (Yamada *et al.* 2010; Takagi *et al.* 2012) and all over Japan (Nakata & Snieder 2012) were detected.

Seismic velocity changes may also occur without strong shaking. Velocity changes related to earthquake swarm activity were measured (Maeda *et al.* 2010; Ueno *et al.* 2012). Even for the 2006 slow-slip event in the Guerrero region of Mexico, velocity changes were detected (Rivet *et al.* 2011).

In this paper, we will focus on single-station cross-correlation (SC) and AC and compare the results with CCs. In general, CC means to correlate the signals of two distinct stations. In this case,

the first station acts as a virtual source and the Green's function describes waves leaving the first station, travelling around and finally arriving at the second station. A CC function thus includes both direct waves and singly or multiply scattered waves. Waves travelling from the second station to the first station are measured in negative times. The signal of a single station can be correlated with itself. This is called AC. An AC function does not exhibit direct waves, but only singly and multiply scattered waves. As modern seismic sensors have three independent components, it is also possible to combine ACs and CCs by cross-correlating the different sensor components, as was for example applied by Wegler *et al.* (2009) or more recently by Zhao *et al.* (2012). It is possible to improve this method by whitening the signals spectrally before cross-correlating the different sensor components. We will call this improved processing technique single-station cross-correlation.

The three different types of correlations have different advantages and disadvantages. Using the CC technique, it is possible to calculate 18 independent correlations for each station pair as the three components of the first station can be correlated with the three components of the second station. Furthermore, waves can travel in both directions, that is, from the first to the second station and vice versa (negative and positive times in the correlation function). By combining all 18 possible correlations, the velocity change estimation can be largely stabilized (Hobiger *et al.* 2012), leading to very robust velocity variation estimations. For the AC technique, only three independent correlations can be calculated (EE, NN and ZZ), the signals for negative and positive times of the correlation function are identical. The SC technique with six independent correlations (EN, NZ and ZE with different negative and positive times) is between the other two techniques in terms of robustness of the final results.

A main disadvantage of the AC is that, in contrast to the other techniques, spectral whitening of the signals before the correlation is not possible. Indeed, by whitening the signal, the amplitude of the signal is set to 1 for all frequencies, so only the phase of the signal remains. However, correlating such a signal with itself (*cf.* eq. 1) results in a perfect delta peak which does not carry information on the medium anymore. Therefore, the AC signals are prone to changes of the seismic noise source during the year (at frequencies below 1 Hz) and to human activities such as industrial or traffic noise (at frequencies above 1 Hz). If only a single frequency is dominant in the noise, it can still be filtered out, but not in an automatic way. However, if multiple frequencies dominate the signal, there is no effective way to clean the signal and the AC analysis will be biased. For both CC and SC, in contrast, the spectra can be whitened before the correlation calculation.

A main limitation of the CC technique is the distance between the different sensors. If two sensors are located too far away from each other (on the order of the typical attenuation length), the signals recorded at both sensors are not coherent anymore and therefore the correlation fails. For example, direct waves in the frequency range above 0.5 Hz are clearly visible for stations closer than about 40 km only (Hobiger *et al.* 2012).

In this paper, we will apply the SC and AC analysis to three and a half years of continuous seismic ambient noise recorded in the area around the Iwate-Miyagi Nairiku earthquake and compare the results with the results of the CC analysis. The data include the Iwate-Miyagi Nairiku earthquake and the Tohoku earthquake. We will analyse the velocity variation curves of the different stations in different frequency ranges and compare the coseismic velocity changes caused by both earthquakes. For the Iwate-Miyagi earthquake, we will analyse the post-seismic recovery of the seismic velocities and attempt to separate velocity changes which recover over the observation timescale from changes not recovering during the observation time. Furthermore, we will analyse seasonal velocity variations occurring at the different stations.

2 DATA SET

For this study, we analyse the data of seventeen Hi-net borehole stations operated by the National Research Institute for Earth Science and Disaster Prevention (NIED) and three surface stations operated by the Japan Meteorological Agency (JMA). A map of the station locations with respect to the epicentre and fault zone of the 2008 Iwate-Miyagi Nairiku earthquake (2008 June 13) is shown in Fig. 1. Continuous data from 2008 January 1 to 2011 June 30 are analysed. At the time of the 2008 Iwate-Miyagi Nairiku earthquake, all stations were operational. With one exception, they also recorded around the 2011 Tohoku earthquake.

3 DATA PROCESSING

3.1 Calculation of SCs and ACs

The correlation functions are calculated on an hourly basis. First, the time-series $X_Z(t)$, $X_E(t)$ and $X_N(t)$ for the vertical, eastern and northern components, respectively, are read. In the case of SC, the data are then whitened spectrally, that is, they are Fourier-transformed, the amplitudes are set to 1 and the data are retransformed in the time domain by an inverse Fourier transform. For ACs, this step is omitted.

In the next step, the data are filtered in five different frequency ranges (0.125–0.25 Hz, 0.25–0.5 Hz, 0.5–1.0 Hz, 1.0–2.0 Hz, 2.0–4.0 Hz). The final correlation functions are calculated in the frequency domain by an equation equivalent to the time-domain formulation

$$C_{k_1 k_2}(t) = n \cdot \int \mathrm{sgn}\left[X_{k_1}(\tau)\right] \cdot \mathrm{sgn}\left[X_{k_2}(\tau - t)\right] \mathrm{d}\tau, \quad (1)$$

where k_1 and k_2 stand for the components Z, E and N and n is a normalization constant setting the maximum possible value for $C_{k_1 k_2}(t)$ to 1. The sgn function stands for the 1-bit normalization, amplifying low-amplitude data such as ambient seismic noise with respect to high-amplitude data such as earthquake signals. In eq. (1), $k_1 = k_2$ for AC and $k_1 \neq k_2$ for SC. The different 1-hour correlation functions for each day are averaged and only these daily correlation functions are stored.

3.2 Daily velocity variations

In order to stabilize the correlation functions, it is necessary to smooth them over a time range depending on the frequency range. In the different frequency ranges, we smoothed over 30 d (0.125–0.25 Hz), 20 d (0.25–0.5 Hz), 10 d (0.5–1.0 Hz), 6 d (1.0–2.0 Hz) and 3 d (2.0–4.0 Hz). The different SC and AC functions for station NRKH, which is located close to the southern part of the fault zone, are shown in Fig. 2 for the frequency range from 0.5 to 1.0 Hz for the whole analysis period. The SC are shown for positive and negative times, whereas the ACs are only shown for positive times because they are by definition the same for negative and positive times. Both SC and AC show phases which are very stable in time. After the 2008 Iwate-Miyagi Nairiku earthquake (the grey area in 2008), a clear offset between the pre-seismic and the post-seismic levels can

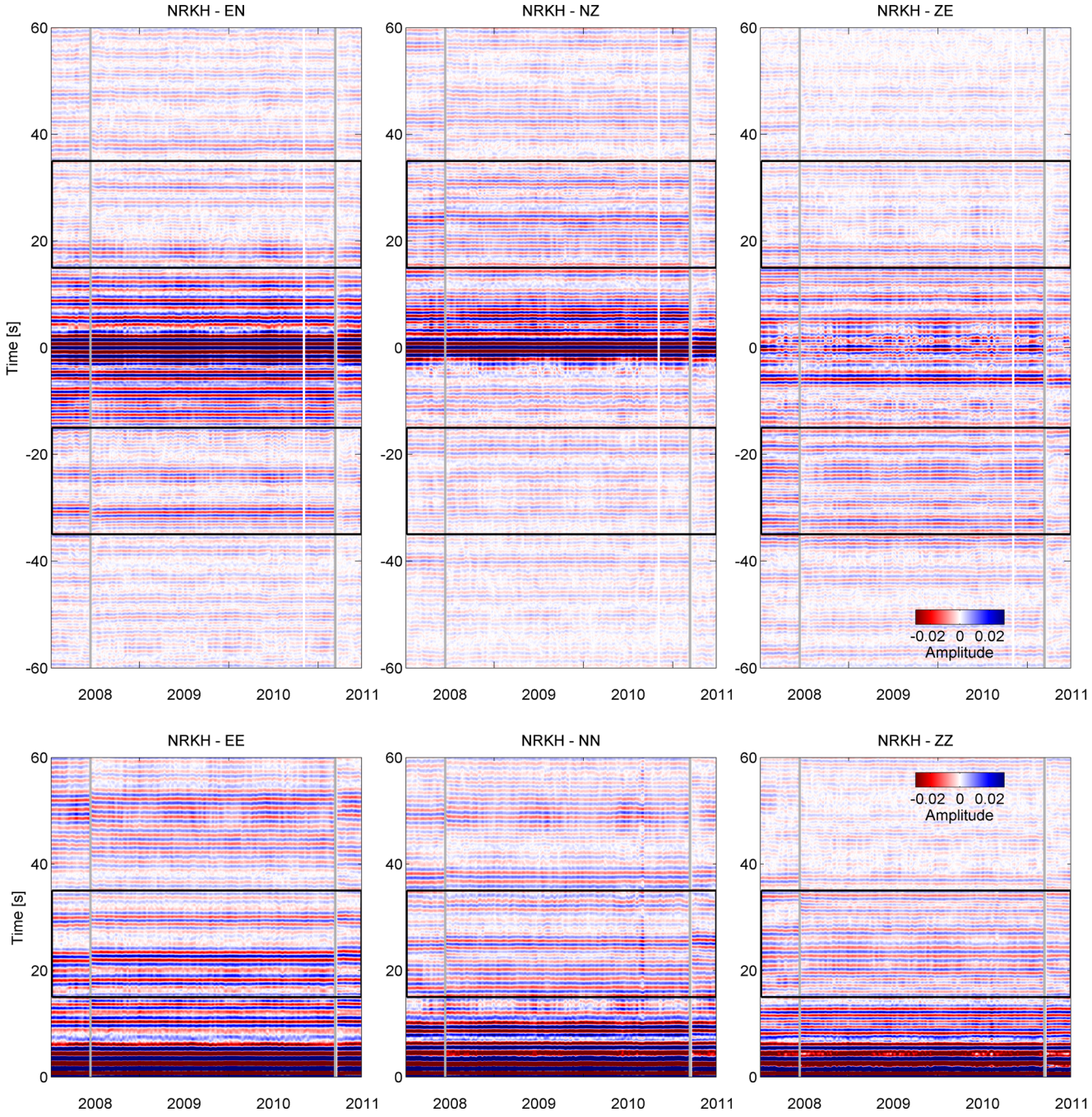

Figure 2. Daily single-station cross-correlation (top row) and auto-correlation (bottom row) functions (smoothed with a 10-d moving average) for station NRKH in the frequency range from 0.5 to 1.0 Hz. As the AC functions are by definition equal for positive and negative times, only their positive time parts are shown. The grey areas indicate the days of the 2008 Iwate-Miyagi Nairiku earthquake and the 2011 Tohoku earthquake, respectively. As the data in these areas include averaged data from before and after the respective earthquakes, they are omitted for clarity reasons. The black rectangles indicate the parts of the correlation functions where the velocity variations have been determined.

be seen in the phases for all correlation functions. After the 2011 Tohoku earthquake, a similar offset is visible. These offsets are a visual evidence for coseismic velocity decreases. The amplitude of the decrease will be determined later. Using the daily correlation functions of Fig. 2, it is possible to measure the actual relative velocity change for each day. Assuming a constant relative velocity change Δ in the medium around the station, every wave propagating from the station to the scatterers and back to the station will be delayed by a relative time delay proportional to the relative velocity change:

$$\Delta = \frac{\mathrm{d}v}{v} = -\frac{\mathrm{d}t}{t}, \tag{2}$$

where $\mathrm{d}v$ is the absolute change of velocity v and $\mathrm{d}t$ is the absolute shift of time t. Consequently, the complete correlation function will be stretched proportionally to Δ (Sens-Schönfelder & Wegler 2006; Wegler *et al.* 2009). Therefore, it is possible to determine Δ by comparing the correlation curve for the specific day with

stretched versions of a reference correlation curve. The sum of all daily correlation curves serves as a reference function in our case. The daily correlation functions are correlated to stretched versions of the reference function (with Δ varying from -5 per cent to $+5$ per cent) in a certain time window for both negative and positive times. In this analysis, time windows of 10 periods length in the coda part starting 7.5 periods after the origin time are selected, where the periods are calculated for the lowest frequency of the respective frequency range. This lag time range is the same as used in Hobiger *et al.* (2012) for the CC analysis. The Δ with the largest correlation coefficient is identified as the relative velocity variation for that day. The correlation coefficient serves as a quality indicator for the relative velocity measurement.

3.3 Comparison of the different components

In Fig. 3, the velocity variations for the correlation curves of Fig. 2 have been determined using the stretching technique. On all components, there is a clear coseismic velocity drop visible at the time of the Iwate-Miyagi Nairiku earthquake, but also a second drop of similar size during the Tohoku earthquake. However, the curves for the different components of the SC (a–f) and the AC (h–j) are a little scattered and do not show exactly the same coseismic velocity drops. By averaging the velocity variations of the different components, the velocity variation can be stabilized. The averaged velocity variation curves $\Delta(t)$ with the respective averaged correlation coefficients $c(t)$ which are shown in Figs 2(g) and (k) have been obtained by

$$\Delta(t) = \frac{\sum_{k=1}^{N} c_k^2(t) \cdot \Delta_k(t)}{\sum_{k=1}^{N} c_k^2(t)}, \tag{3}$$

$$c(t) = \frac{\sum_{k=1}^{N} c_k^3(t)}{\sum_{k=1}^{N} c_k^2(t)}, \tag{4}$$

where the relative velocity variation of a single component is denoted by $\Delta_k(t)$ and the corresponding correlation coefficient by $c_k(t)$ ($k \in [1, 2, \ldots, N]$ indicates the different component combinations, that is, EN^+, EN^-, $\ldots$, ZE^- for SC and EE, NN and ZZ for AC). For SC, $N = 6$, and for AC, $N = 3$. According to eq. (4), $c(t) \leq \max(c_k(t))$.

For station NRKH, the coseismic velocity drops of the Iwate-Miyagi Nairiku earthquake range from -0.65 per cent to -0.84 per cent for the different SC components and from -0.71 to -0.91 per cent for the AC component combinations. For this station, the velocity changes for the different combinations are in rather good agreement, but for other sites, there are larger differences.

Fig. 4 shows the respective velocity change curves for station ICEH in the same frequency range. For this station, the coseismic velocity drops of the Iwate-Miyagi Nairiku earthquake range from -0.24 to -0.57 per cent for SC and from -0.26 to -0.57 per cent for AC. The differences in the components may be caused by the different propagation paths of the respective seismic waves. For example, the EN combination is sensitive to Rayleigh and Love waves, to shear waves travelling downwards and coming back after reflection at depth and also to pressure waves. The NZ and ZE combinations, however, are not sensitive to Love waves. Therefore, different depth sensitivities of Rayleigh and Love waves together with differences of the velocity changes with depth may explain the differences in the component combinations. An inhomogeneous velocity change distribution in the area together with different ray paths are another probable explanation for the differences in the component combinations. At the end of 2008 and the beginning of

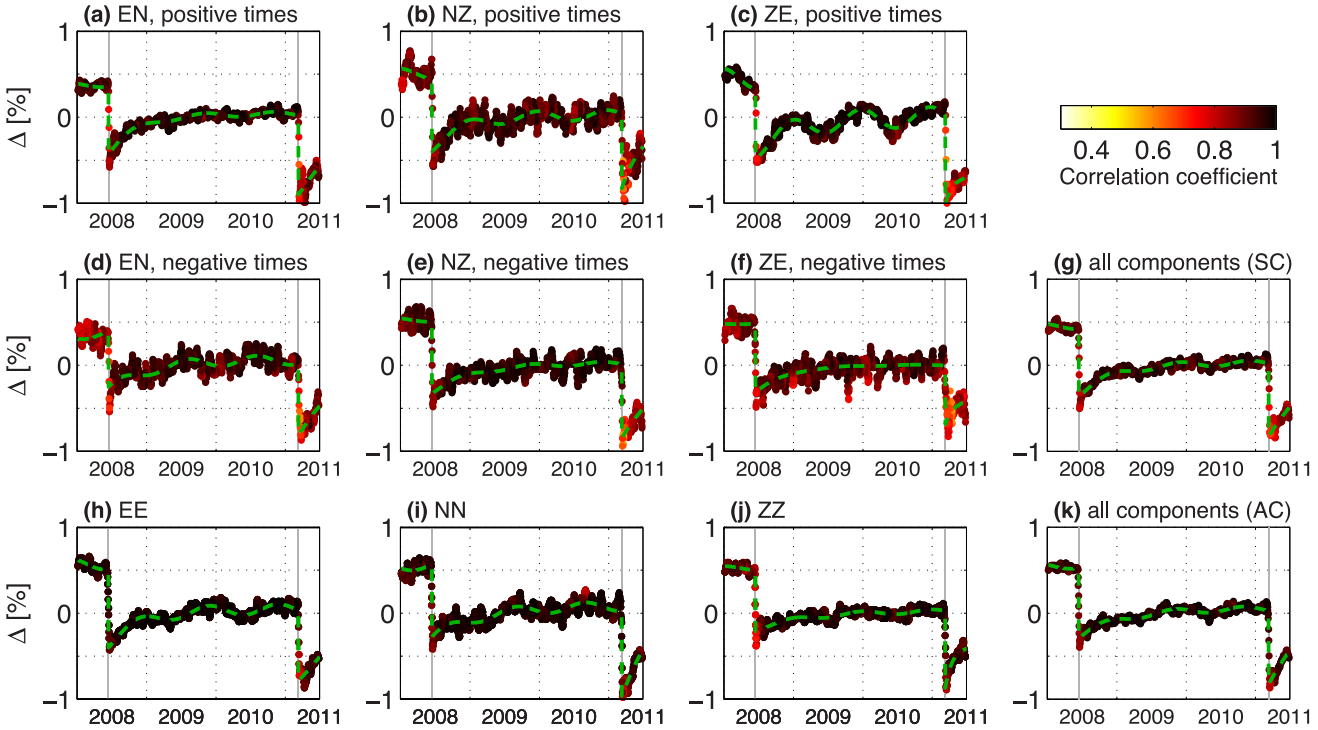

Figure 3. Velocity variation curves for the different components of the SC analysis (a–f), the average of these curves (g), the differents components of the AC analysis (h–j) and the average of these curves (k), all in the frequency range from 0.5 to 1.0 Hz and for the station NRKH. The grey lines indicate the dates of the 2008 Iwate-Miyagi Nairiku earthquake and the 2011 Tohoku earthquake. The green dotted lines are fitted curves described by eq. (5).

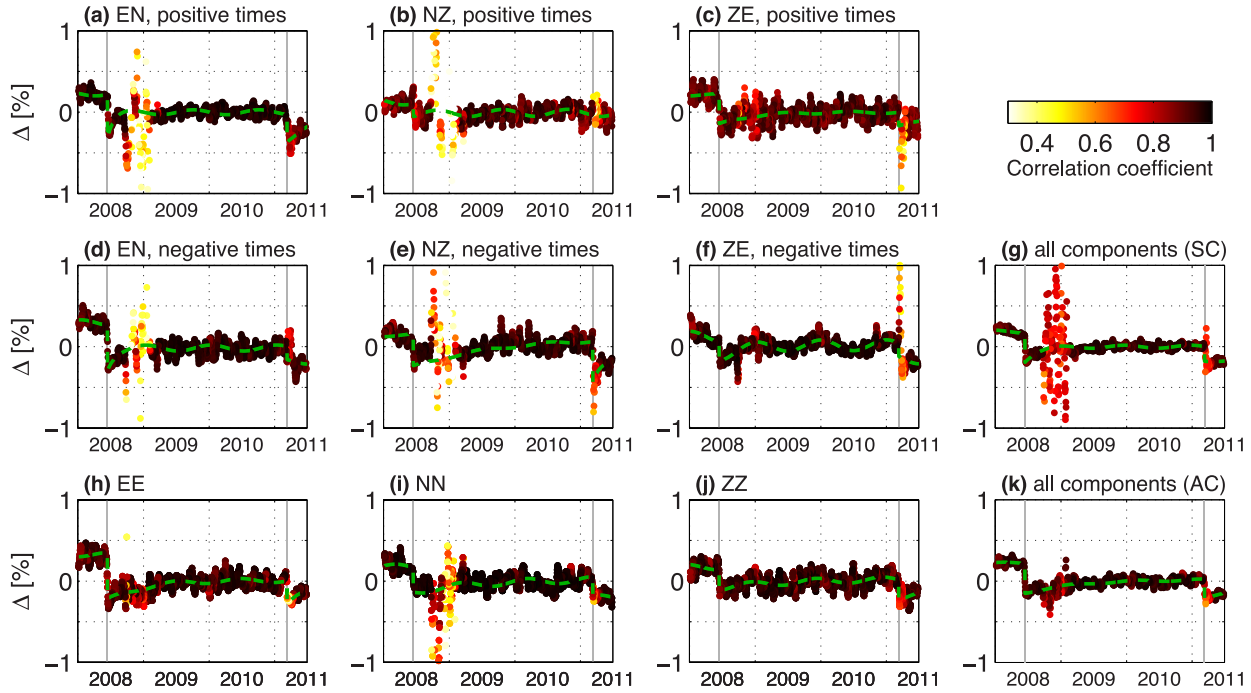

Figure 4. The same as Fig. 3, but for station ICEH.

2009, the data quality of the northern component of station ICEH was poor. This problem is visible on all curves which include the northern component. As two thirds of the SC components include this component, the data problem is also visible in the resulting average curve. Only one third of the AC components have this data problem and the resulting average is more robust against such data problems.

The velocity variation curves averaged over the different component combinations are more stable than the single component combinations. In the following, we will only use velocity change curves averaged over the different components for both SC and AC.

3.4 Curve fitting

In Fig. 3, there are green dotted curves which were fitted to the data. These curves are described by

$$f(t) = A + \left[B + C \cdot \exp\left(-\frac{t-t_1}{D}\right)\right] \cdot H(t-t_1) + \left[E + F \cdot \exp\left(-\frac{t-t_2}{G}\right)\right] \cdot H(t-t_2) + J \cdot \sin(\omega t) + K \cdot \cos(\omega t), \quad (5)$$

where A, B, C, D, E, F, G, J and K are the nine fit parameters, $H(t)$ is the Heaviside function [i.e. $H(t \geq 0) = 1$ and $H(t < 0) = 0$]. t_1 is the time of occurrence of the 2008 Iwate-Miyagi Nairiku earthquake, t_2 the date of the 2011 Tohoku earthquake. ω in the sine and cosine terms is fixed to be 2π yr^{-1}. The first parameter, A, is just a constant offset. B, C and D describe a coseismic velocity change and post-seismic recovery caused by the Iwate-Miyagi Nairiku earthquake, where B is a velocity change which does not recover during the observation time (therefore in the following called non-recovering velocity change) and C is a coseismic velocity change recovering on an exponential scale with time constant D. The total coseismic velocity change is thus $B + C$. Analogously, E, F and G are the parameters describing coseismic and post-seismic velocity changes of the Tohoku earthquake. The last two parameters, J and K, describe seasonal velocity variations with periods of exactly one year. These two terms can be combined into a single cosine term by

$$J \cdot \sin(\omega t) + K \cdot \cos(t) = \sqrt{J^2 + K^2} \cdot \cos[\omega t - \tan^{-1}(J/K)], \quad (6)$$

where $\sqrt{J^2 + K^2}$ is the amplitude and $\tan^{-1}(J/K)$ the phase of the seasonal velocity variations. The phase can be easily given in days instead of degrees and indicates at which day of the year the velocity maximum occurs.

The different parameters of eq. (5) can be obtained by a non-linear least-squares fit to the observed data $\Delta(t)$, minimizing

$$\chi^2 = \frac{\sum_{i=1}^{N_D} [c(t_i)]^2 [f(t_i) - \Delta(t_i)]^2}{\sum_{i=1}^{N_D} [c(t_i)]^2}, \quad (7)$$

where t_i indicates the observation days and $c(t_i)$ is the measured correlation coefficient on day t_i, here serving as a weighting factor. The sums span over all N_D days of observation, in our case 1277 d. In this way, the χ^2 of eq. (7) indicates the average squared difference between the measured data points and the fitted curve.

4 RESULTS

4.1 Velocity variations at different frequencies

In Fig. 5, examples of velocity variation curves at different frequencies are shown. These curves have been obtained with the SC, AC and CC techniques, each time after combining all respective component combinations. The CC results are shown for the

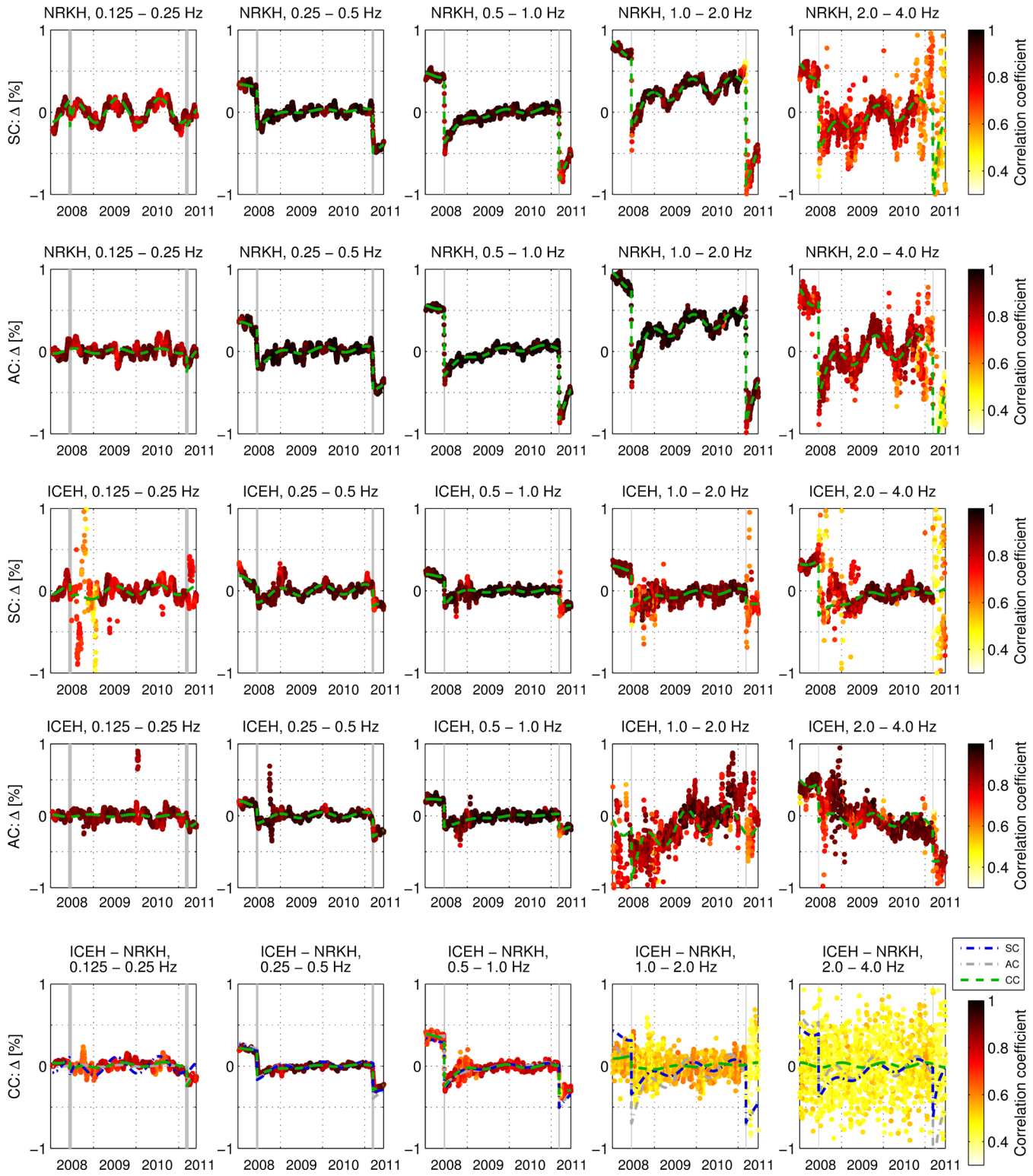

Figure 5. First line: the SC velocity variations for station NRKH in five different frequency ranges. Second line: the respective AC velocity variations for station NRKH. Third and fourth lines: the respective SC and AC velocity variations of station ICEH. Fifth line: the CC velocity variation curves between stations ICEH and NRKH. The dash–dotted blue and grey lines correspond to the corresponding velocity variation curves expected from the SC and AC results, respectively. They correspond to the average of the respective curves for stations NRKH and ICEH.

station pair ICEH-NRKH. SC and AC results are shown for both stations. Station ICEH is located east of the central part of the fault zone, station NRKH is located in the west of the southern part of the fault zone. The distance between both stations is 32.7 km, the direct ray path between both stations directly crosses the part of the fault zone where Ohta *et al.* (2008) located the largest coseismic slip during the Iwate-Miyagi Nairiku earthquake. The green dotted lines in Fig. 5 have been obtained by a nonlinear fit of

Table 1. Properties of the model curves fitted to the velocity variation curves in Fig. 5 using eq. (5). The parameters B and E of the coseismic velocity changes describe non-recovering changes. C and F are coseismic changes with recovery times D and G, respectively. The average correlation coefficients are averaged over all component combinations for the respective correlation technique.

Correlation		Frequency range (Hz)	Coseismic velocity change Iwate-Miyagi Nairiku			Coseismic velocity change Tohoku			Seasonal variations Amplitude (per cent)	Seasonal variations Phase (d)	χ (per cent)	Average corr. coeff.
Parameter in eq. (5):			B (per cent)	C (per cent)	D (yr)	E (per cent)	F (per cent)	G (yr)	$\sqrt{J^2+K^2}$	$\tan^{-1}(\frac{J}{K})$		
NRKH	SC	0.125–0.25	−0.01	−0.30	0.1	−0.08	0.00	1.5	0.15	189	0.06	0.82
NRKH	SC	0.25–0.5	−0.30	−0.20	0.4	0.00	−0.52	1.0	0.02	360	0.04	0.93
NRKH	SC	0.5–1.0	−0.43	−0.36	0.5	0.00	−0.85	0.5	0.03	329	0.04	0.93
NRKH	SC	1.0–2.0	−0.44	−0.45	0.6	0.00	−1.20	0.5	0.10	324	0.06	0.89
NRKH	SC	2.0–4.0	−0.45	−0.46	1.0	0.00	−1.26	0.1	0.12	310	0.21	0.74
NRKH	AC	0.125–0.25	0.00	0.00	0.8	0.00	0.00	0.1	0.03	193	0.07	0.86
NRKH	AC	0.25–0.5	−0.29	−0.18	0.5	0.00	−0.54	0.8	0.04	4	0.05	0.95
NRKH	AC	0.5–1.0	−0.50	−0.32	0.6	0.00	−0.86	0.5	0.03	300	0.03	0.96
NRKH	AC	1.0–2.0	−0.47	−0.49	0.7	−0.14	−1.11	0.4	0.10	335	0.06	0.95
NRKH	AC	2.0–4.0	−0.65	−0.54	0.4	−0.38	−1.86	0.1	0.15	295	0.16	0.78
ICEH	SC	0.125–0.25	0.00	−0.15	0.5	0.00	0.00	0.5	0.06	170	0.09	0.77
ICEH	SC	0.25–0.5	−0.11	−0.11	0.6	−0.13	−0.10	0.1	0.06	359	0.04	0.90
ICEH	SC	0.5–1.0	−0.18	−0.14	0.5	−0.11	−0.07	1.3	0.02	332	0.03	0.93
ICEH	SC	1.0–2.0	−0.27	−0.15	0.8	−0.11	−0.08	0.1	0.04	1	0.07	0.85
ICEH	SC	2.0–4.0	−0.33	−0.33	0.8	0.00	0.00	0.7	0.04	239	0.21	0.81
ICEH	AC	0.125–0.25	0.00	0.00	1.4	0.00	−0.20	0.3	0.02	326	0.10	0.87
ICEH	AC	0.25–0.5	−0.16	−0.08	0.4	0.00	−0.32	0.4	0.04	353	0.06	0.92
ICEH	AC	0.5–1.0	−0.20	−0.17	0.8	0.00	−0.25	0.6	0.01	46	0.05	0.94
ICEH	AC	1.0–2.0	0.00	−0.76	0.5	0.00	0.00	0.1	0.21	278	0.44	0.82
ICEH	AC	2.0–4.0	−0.55	0.00	0.5	−0.49	0.00	0.7	0.09	276	0.20	0.84
ICEH-NRKH	CC	0.125–0.25	−0.04	−0.08	0.4	−0.14	−0.10	0.1	0.03	240	0.05	0.75
ICEH-NRKH	CC	0.25–0.5	−0.20	−0.11	0.7	−0.14	−0.16	0.5	0.01	319	0.02	0.88
ICEH-NRKH	CC	0.5–1.0	−0.37	−0.23	0.3	−0.26	−0.07	0.1	0.02	339	0.04	0.76
ICEH-NRKH	CC	1.0–2.0	−0.04	−0.11	2.6	0.00	0.00	0.5	0.02	191	0.14	0.54
ICEH-NRKH	CC	2.0–4.0	0.00	0.00	0.1	0.00	0.00	1.0	0.03	2	0.33	0.47

eq. (5) to the data. The parameters of these fits are indicated in Table 1.

When comparing the SC and AC curves for station NRKH (first and second line in Fig. 5), there are large differences in the lowest frequency range. The SC exhibits very strong seasonal variations and a rather strong, but quickly recovering coseismic velocity decrease during the Iwate-Miyagi Nairiku earthquake. Both features are not visible in the AC. In the three frequency ranges between 0.25 and 2.0 Hz, however, the SC and AC curves are extremely similar and also the fit parameters are very close. In the highest frequency range, the overall correlation quality decreases and the velocity variations are very scattered. The main properties of the SC and AC curves are still comparable, but larger differences appear, for example, the size of the coseismic velocity drop caused by the Iwate-Miyagi Nairiku earthquake. Overall, we can observe an increase of the coseismic velocity changes for both earthquakes with frequency for SC and AC. Furthermore, the coseismic changes (i.e. the sum of B and C or E and F, respectively, see Table 1) for both earthquakes are very similar in size, with slightly larger changes for the Tohoku earthquake. In the lowest frequency range, the coseismic velocity drops are not significant. For the higher frequency ranges, the absolute size of the coseismic drops caused by the Iwate-Miyagi Nairiku earthquake increases monotonously and finally reaches 0.90 per cent for the SC and 1.19 per cent for the AC in the highest frequency range. For the Tohoku earthquake, a comparable monotonous increase is visible. Seasonal velocity variations are strongest at the lowest frequency range (below 0.25 Hz) and at frequencies above 1.0 Hz, but of lower amplitude for the intermediate frequencies.

For station ICEH (third and fourth line in Fig. 5), the qualitative results are similar. In the lowest frequency range, the AC is more stable and shows less seasonal variations than the SC. In the next two frequency ranges, that is, from 0.25 to 1.0 Hz, the SC and AC results are very similar. In the fourth frequency range between 1.0 and 2.0 Hz, however, the SC still gives a stable velocity variation curve with visible coseismic velocity drops for both earthquakes, but the data quality is worse than at lower frequencies, as is also indicated by the larger value of χ in this case. In the fifth frequency range, apart from some scattered data points of low correlation quality, the SC still gives a curve with the same, at least partly recognizable features as for the lower frequencies. However, the ACs in both the fourth and fifth frequency ranges give very unstable curves with much scattering. It is difficult to determine meaningful coseismic velocity drops for such curves. Overall, an increase of the coseismic velocity drops with frequency can also be observed for this station, but the coseismic velocity drops are smaller than for station NRKH. However, the coseismic drops are larger during the Iwate-Miyagi Nairiku earthquake than during the Tohoku event. For the Iwate-Miyagi Nairiku earthquake, a monotonous increase of the size of the coseismic velocity drops can be seen, similar to station NRKH. For the Tohoku event, however, the coseismic drops are around 0.2 per cent for all frequency ranges between 0.25 and 2.0 Hz. At higher frequencies, the correlation coefficients of the data are too poor after this earthquake to determine a reliable value for

coseismic changes here. Seasonal velocity variations are lower than at NRKH, but here again, they are less significant at intermediate than at lower and higher frequencies.

In the CC analysis (fifth line in Fig. 5), the curves in the lowest three frequency ranges are very proper and stable. In the frequency range between 1.0 and 2.0 Hz, however, the correlation quality becomes poor. This problem is often encountered in CC analysis. As the frequency increases, the coherence between the signals at both stations decreases. In this case, both stations are too far away from each other to get a significant CC. Going to the next higher frequency range further increases this problem. In the three high-quality frequency ranges, the coseismic velocity changes increase monotonously for both earthquakes. Seasonal velocity variations are only small. In our previous publication (Hobiger *et al.* 2012), we analysed CCs and developed a tomography algorithm to reproject the velocity changes measured for the different station pairs onto the positions of the single stations. This algorithm is based on a simplification of the sensitivity kernels of Pacheco & Snieder (2005, 2006). They showed that the CC function for a station pair is mainly sensitive to the close surroundings of the single stations. The simplification was to assume that the observed velocity change for a station pair will then be the average of the actual velocity changes at the two stations. For station pair ICEH-NRKH, this would result in

$$\Delta_{\mathrm{ICEH-NRKH}} = (\Delta_{\mathrm{ICEH}} + \Delta_{\mathrm{NRKH}})/2. \quad (8)$$

As we have measured the velocity change curves for both stations with the SC and AC techniques, we can use them to calculate the theoretical CC velocity variation curve for the station pair using eq. (8). In the lowest line of Fig. 5, these curves are plotted together with the CC fit curve. In the lowest frequency range, there is a good agreement between the AC and CC curves, the SC shows too much seasonal variations. In the intermediate frequency ranges, that is, between 0.25 and 1.0 Hz, the agreement between all three curves is striking. In the higher frequency ranges, however, the poorly measured CC curve cannot be compatible with the other two correlation techniques.

4.2 Overview of coseismic velocity variations

4.2.1 Coseismic velocity changes caused by the Iwate-Miyagi Nairiku earthquake

Our goal in the following is to give an overview of the velocity variations in the study area instead of focusing on single stations. As SC and AC are single-station techniques, it is very simple to plot the respective velocity changes of the different stations on a map of the study area. For the coseismic velocity changes of the Iwate-Miyagi Nairiku earthquake, such maps are shown in Fig. 6 for four frequency ranges between 0.125 and 2.0 Hz. The presented velocity changes are determined using the nonlinear fit and are given by the sum of parameters B and C of eq. (5). The χ of the fitting procedure may serve as a quality control of the fit, as it indicates the average distance between the fit curve and the data points. In order not to introduce biases due to bad data, we set the quality criterion to $\chi = 0.11$ per cent and omitted all data with higher χ in the overview

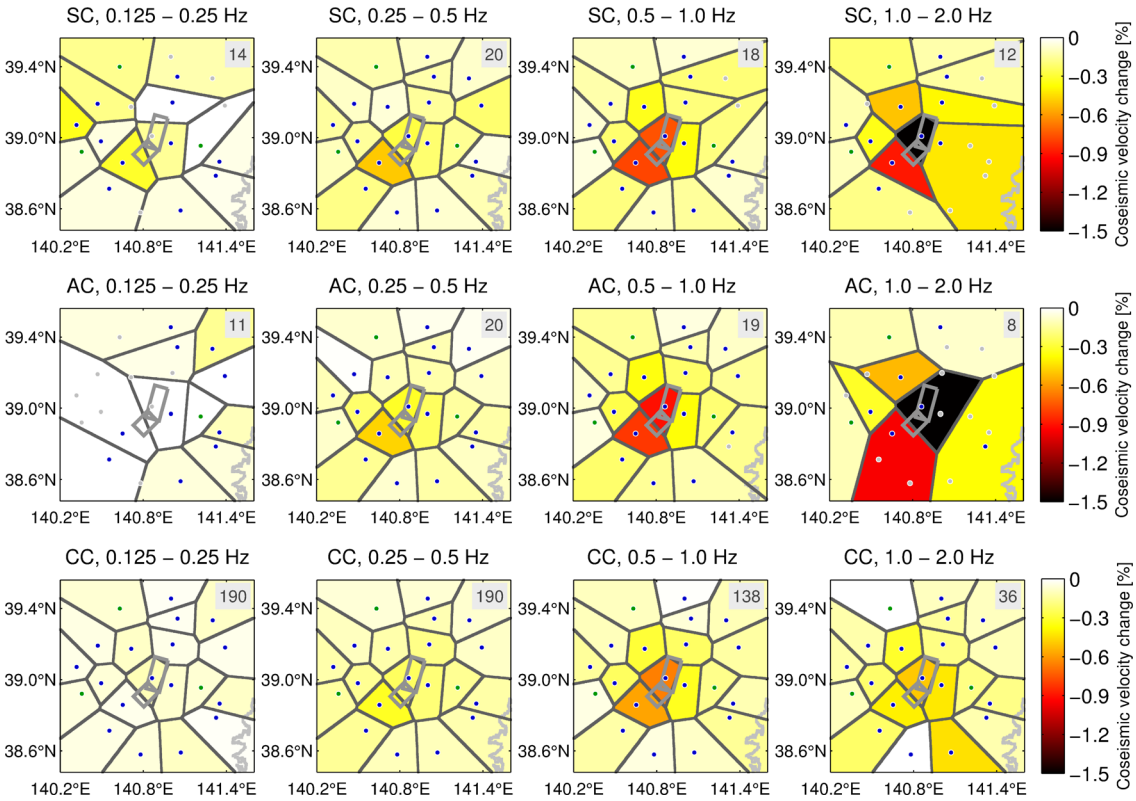

Figure 6. Coseismic changes caused by the 2008 Iwate-Miyagi Nairiku earthquake in different frequency ranges and for different correlation methods: SC, AC and CC (from top to bottom). The small number in the upper right corner is the number of stations or station pairs with data of good quality ($\chi < 0.11$ per cent). Only the data of these stations are used for the figures. These stations are indicated by coloured dots in the figures, the other station locations are given by grey dots. The areas surrounding the good quality stations are coloured according to the velocity changes of these stations, the borders between the different areas are determined by a closest neighbour approach.

plots. Instead of interpolating the data, the maps represent a kind of tesselation, where each point on the map is attributed to the closest station. In this way, each station is surrounded by an area with a constant velocity change. Consequently, the actual measurement data are highlighted without introducing interpolation bias. The station locations are indicated by the coloured dots, stations which were omitted due to poor data quality are indicated by light grey dots.

In the SC results (first line of Fig. 6), a general trend of increasing coseismic velocity changes with frequency is visible. The strongest velocity changes occur close to the fault zone. The AC analysis (second line of Fig. 6), gives very similar results, especially for the frequencies between 0.25 and 1.0 Hz. In the lowest frequency range, there are two stations with coseismic changes of about −0.3 per cent in the SC analysis, which do not show such strong velocity changes in the AC analysis. However, both stations also show a very fast recovery with a time constant of 0.1 yr. Between 1.0 and 2.0 Hz, the velocity changes for the different stations with good data quality are in good agreement, the difference in the figures is caused by different stations giving good results in both techniques. In the third line of Fig. 6, the results of the CC analysis of our previous study (Hobiger *et al.* 2012) are shown. In contrast to the SC and AC figures, these results are obtained after the application of the tomography algorithm to the different station pairs' velocity changes. Therefore, even if all station pairs do not give good results with low χ, the tomography will give a result for each station which has at least one good quality pair with another station. This limits the significance in the highest frequency range shown, where only 36 of 190 station pairs gave good correlations. In the three lowest frequency ranges, the results are in rather good agreement with the other techniques. The coseismic velocity drops increase with frequency. In the lowest frequency range, only minor velocity drops are observed. At higher frequencies, larger coseismic changes are mainly located close to the fault zone. However, the CC velocity changes are slightly smaller than the SC and AC changes. The CC results between 1.0 and 2.0 Hz are very similar to the third frequency range, but differ largely from the SC and AC results. This might be caused by the lower data quality and thus tomography quality in this frequency range.

4.2.2 Coseismic velocity changes caused by the Tohoku earthquake

The coseismic velocity changes caused by the Tohoku earthquake are shown in Fig. 7 for the three correlation methods. Here again, the SC and AC results are very similar with slight differences in the lowest frequency range. The CC results differ a bit more, but are still in fair agreement with the other techniques in the lowest three frequency ranges. Also for this earthquake, the size of the velocity changes increases with frequency, but even at the lowest frequency range, a velocity drop of about 0.3 per cent can be observed. Between 0.25 and 0.5 Hz, all stations show velocity changes of about the same size, except for station NRKH (see also Fig. 5) which exhibits a velocity drop of over 0.5 per cent for SC and AC. In the next highest frequency range, this station also has the strongest velocity drop, but other stations, mainly in the northeast and south, also show large velocity drops. Anyhow, there is no clear spatial distribution of the coseismic velocity changes. In the CC analysis, the velocity changes are smoother and more homogeneous, probably because the tomography algorithm also smoothes the data by averaging over the different station pairs. In the fourth frequency range, the CC analysis detects much smaller changes than the other two techniques, but this might be caused by the above-mentioned problem that most station pairs have bad data quality in this frequency range.

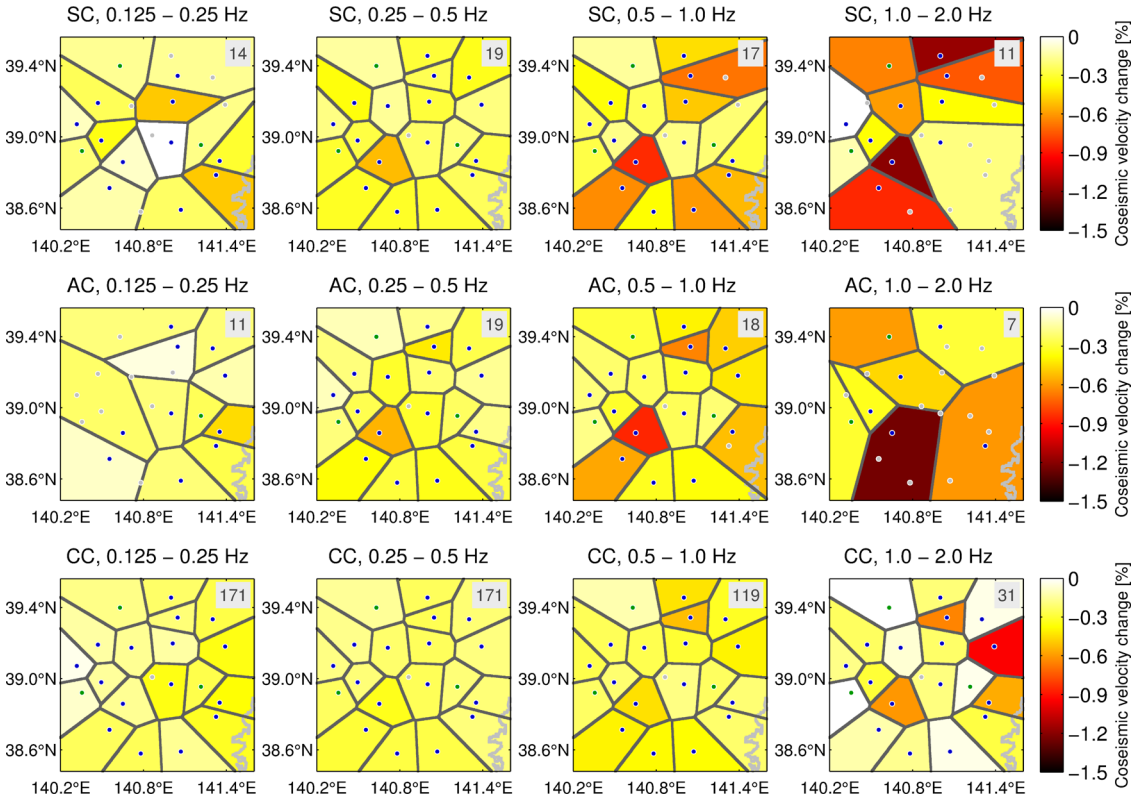

Figure 7. The same as Fig. 6, but for the 2011 Tohoku earthquake.

4.2.3 Separation of recovering and non-recovering coseismic velocity changes, recovery time constants

Using the exponential model of eq. (5) for fitting the seismic velocity variations, the coseismic velocity changes can be separated into a non-recovering (parameter B) and a recovering (parameter C) change. Using a logarithmic model instead of the exponential model actually fits the data in a comparable way (Hobiger *et al.* 2012). However, as the sum of a constant and a logarithmic change results in another logarithmic change, the separation of non-recovering and recovering coseismic changes is not possible with a logarithmic model. In Fig. 8, the non-recovering and recovering parts of the coseismic velocity changes of the Iwate-Miyagi Nairiku earthquake are compared for the SC results. The other correlation techniques give similar results. In the lowest frequency range, there are almost no non-recovering coseismic velocity changes. In the higher frequencies, the amplitudes of recovering and non-recovering velocity changes are quite similar. However, the non-recovering parts of the strong coseismic changes around the fault zone are slightly larger than the recovering parts. For stations more distant from the fault zone, most of the coseismic changes are recovering. With this separation of recovering and non-recovering coseismic changes it might in principle be possible to separate effects on different timescales. Actually, as aforementioned, 'non-recovering' means that the velocity changes are not significantly recovering over the observation time of several years, but they are supposed to recover over much larger timescales. Anyhow, with the results of Fig. 8, it is difficult to really find a good interpretation of the separation results.

Fig. 8 also shows the time constants of the recovering velocity changes of the Iwate-Miyagi Nairiku earthquake, as determined by the nonlinear fit to the SC velocity variation curves. The recovery time corresponds to parameter D in eq. (5). This parameter indicates after which time the coseismic velocity drop has recovered to $1/e$, that is, about 37 per cent of its original value. In order to prevent the fitting of very strong velocity drops with very fast recovery times, the minimum recovery time allowed in the fit process was fixed to 0.1 yr. In the lowest frequency range, the coseismic velocity drops are very small. The obtained recovery times are therefore rather imprecise. The two stations with stronger velocity drops in the lowest frequency range have recovery times of 0.1 yr. In the higher frequency ranges, there are some stations showing very long recovery times, but all of these stations had very small coseismic velocity drops. For the stations with large coseismic drops, the recovery times are always lower than one year. Therefore, it can be stated that the recovering part of the coseismic velocity drops has a typical recovery time of about 0.5 yr.

The fit eq. (5) also gives values for the sizes of the non-recovering (E) and recovering (F) coseismic velocity changes for the Tohoku earthquake and the recovery time (G) of these changes. However, as we analysed less than four months of data after the 2011 Tohoku earthquake, the post-seismic recovery process has not yet finished after this time and a separation of recovering and non-recovering effects is not very precise. The same holds for the recovery time constant. Therefore, we do not attempt to separate the recovering and non-recovering effects of the Tohoku earthquake here.

4.3 Seasonal velocity variations

The velocity variation curves of the different stations also exhibit seasonal velocity variations, which have been fitted using

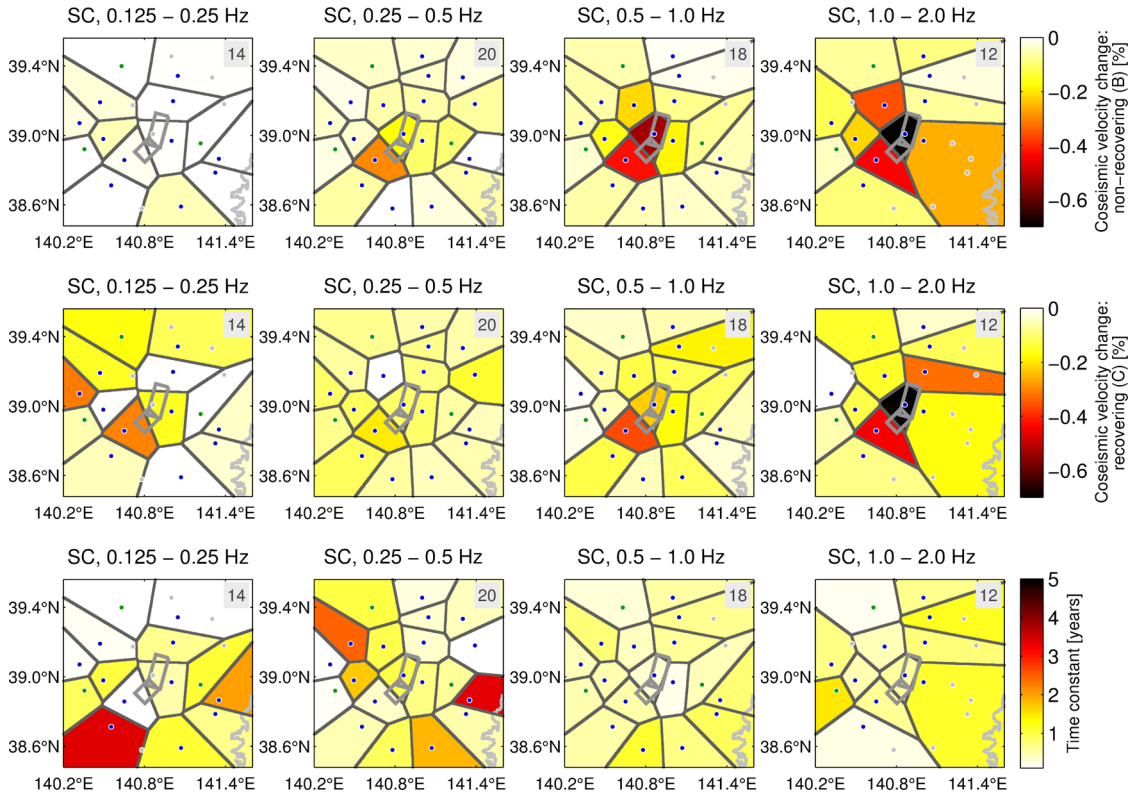

Figure 8. Separation of the SC coseismic velocity changes of the 2008 Iwate-Miyagi Nairiku earthquake in non-recovering changes (parameter B, first line) and recovering changes (parameter C, second line). The recovery time constants (parameter D, third line) of the recovering coseismic velocity changes are also shown. The small number in the upper right corner is the number of stations with good quality data whose data are used in the figure.

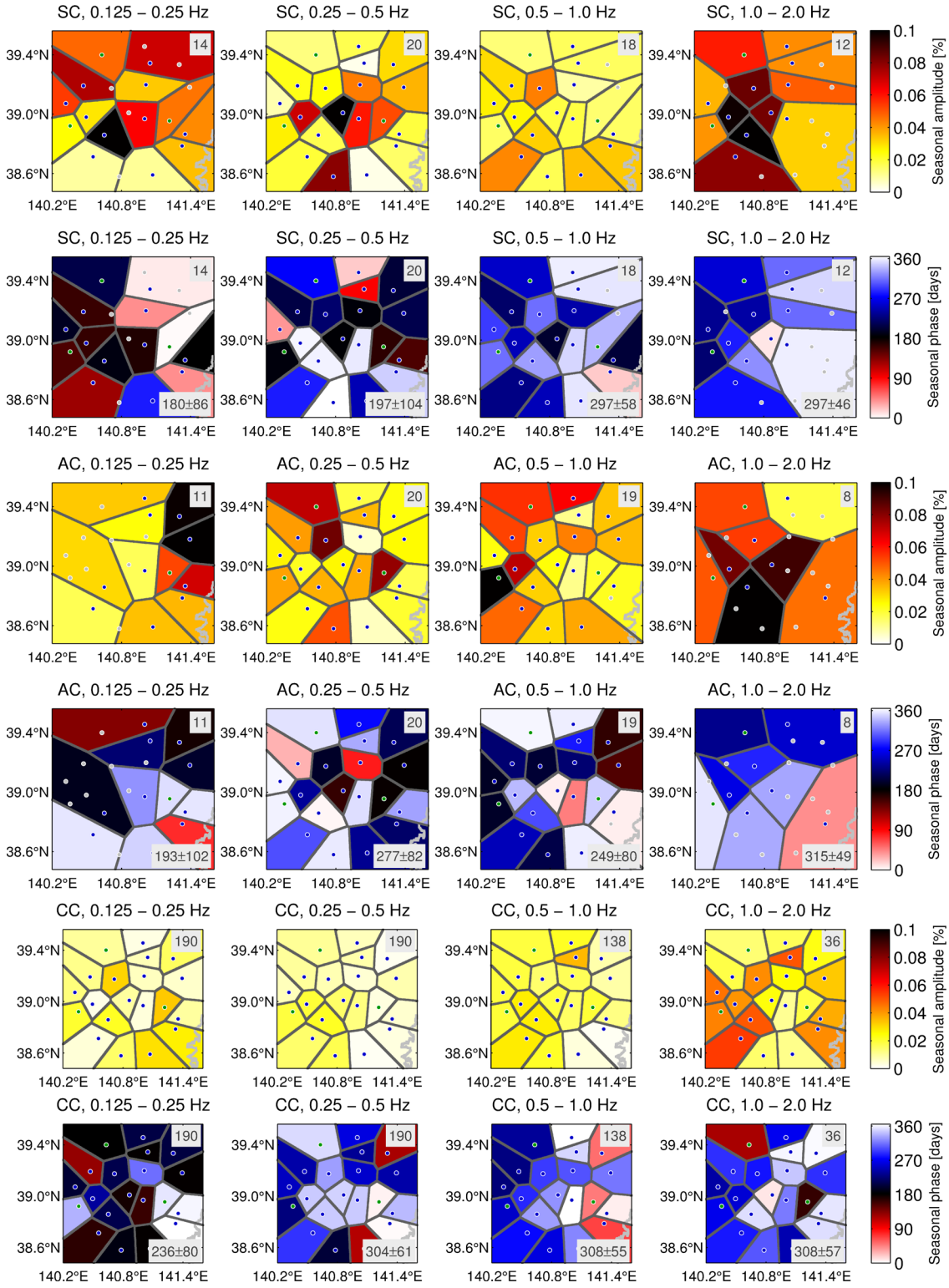

Figure 9. Parameters of the seasonal variations at different frequencies for SC, AC and CC (from top to bottom). For each of the three correlation techniques, the first line shows the amplitude of the seasonal variations and the second line the phase, which is given in days here and indicates the day of year where the seasonal variations are maximum. The small number in the upper right corner is the number of stations or station pairs with good quality data whose data are used in the figure. The number in the lower right corner indicates the average phase of the good quality stations with standard deviation.

parameters J and K in eq. (5). These parameters can be recombined to calculate the amplitude and phase of the seasonal variations according to eq. (6). The phase can be indicated in days and gives the day of the year where the seismic velocity is maximum.

In Fig. 9, the amplitudes and phases of the seasonal variations are shown for the different correlation methods. For SC and AC, the amplitudes do not show any systematic behaviour between the different frequencies. Stations with strong seasonal variations in

one frequency range can show negligible variations in another frequency range. Station NRKH, for example, which has very strong variations in the single-station CCs between 0.125 and 0.25 Hz (see also Fig. 5), has only low seasonal variations between 0.25 and 0.5 Hz and slightly higher variations between 0.5 and 1.0 Hz, but again very strong variations above 1.0 Hz. The amplitudes in the AC analysis are not well related with the SC results. Finally, a significant amplitude difference between the three surface stations (the green dots in Fig. 9) and the 17 Hi-net borehole stations cannot be observed.

For frequencies below 0.5 Hz, there are large phase differences for both SC and AC. In both frequency ranges above 0.5 Hz, the SC phases are more consistent as all stations show velocity maxima in the second half of the year. In both frequency ranges between 0.5 and 2.0 Hz, the average phase (indicated in each plot in the lower right corner) corresponds to a velocity maximum in the end of October. The AC phases in these two frequency ranges are similar, but with some outliers and average phases which are different (earlier between 0.5 and 1.0 Hz, later between 1.0 and 2.0 Hz), but still in agreement when taking the error bars into account.

The amplitudes of the CC analysis, which are only shown after the tomography process here, are much smaller than the SC and AC amplitudes. This can be explained by the tomography itself. The seasonal variations differ a lot between the different station pairs (Hobiger *et al.* 2012). The amplitudes are very different between similar station pairs, but also the phases differ a lot for frequencies below 0.5 Hz. For higher frequencies, the phases are in better agreement for the different station pairs. Applying the tomography algorithm to such data will smooth out a lot of the individual seasonal variation effects, especially for strongly differing phases. This can at least explain the low amplitudes of the CCs at the two lowest frequency ranges. Therefore, the average phases in the two lowest frequency ranges should be taken with caution. Between 0.5 and 1.0 Hz and between 1.0 and 2.0 Hz, however, the phases are more consistent and in quite good agreement with the SCs, as the average phase in these two frequency ranges corresponds to a velocity maximum in early November.

5 ESTIMATION OF THE DEPTH OF THE COSEISMIC VELOCITY CHANGES

With the SC analysis, velocity changes can be measured at higher frequencies than with CCs. Using these data at higher frequencies, we can expect to constrain the depth range of the coseismic velocity changes in a better way than using the CC analysis alone. In Hobiger *et al.* (2012), we tried to determine the depth range using CC measurements in three frequency ranges, between 0.125 and 1.0 Hz. Using the SCs, we can include at least one additional frequency range, that is, between 1.0 and 2.0 Hz, for all stations. For some stations, even the data between 2.0 and 4.0 Hz are good enough to be included in the modelling.

The modelling process is similar to the one used by Hobiger *et al.* (2012). The target is to find a velocity profile explaining the observed coseismic velocity changes $\Delta_{\text{station}}(f)$ the best. In the two frequency ranges below 0.5 Hz, the velocity changes of the CC analysis are used. In the higher frequency ranges, the SC results are used. The average deviation χ obtained by the fitting in eq. (7) is used as standard deviation $\sigma(f)$ for the velocity changes.

The starting point of the modelling is the borehole log of the respective Hi-net station, giving the shallow ground structure down to the Hi-net sensor (data available at http://www.kyoshin.bosai.go.jp; Okada *et al.* 2004). These profiles were extended to larger depths using the velocity and density profiles of J-SHIS (data available at http://www.j-shis.bosai.go.jp; Fujiwara *et al.* 2009). For the three sites with the largest coseismic velocity changes during the Iwate-Miyagi Nairiku earthquake, the resulting shear- and pressure-wave velocity profiles are shown in Fig. 10(a).

As we only have measurements for four or five different frequency ranges, the damage modelling has to be simple and a low number of parameters has to be used. Therefore, we assume two possible parametrizations for the velocity changes. The relative velocity change Δ is assumed constant between the surface and a depth D (assumption 1) or between depths D_1 and D_2 (assumption 2). For the sake of simplicity, we assume in any case that the relative velocity changes of shear- and pressure waves are the same.

Starting from the reference velocity profiles, new profiles are generated by decreasing the seismic velocity by the relative velocity change Δ down to depth D for the first assumption or between depths D_1 and D_2 for the second assumption. The parameter Δ varies between -20 and 0 per cent and the depth parameters D, D_1 and D_2 between –6000 and 0 m (where $D_1 > D_2$). Rayleigh wave (phase velocity) dispersion curves are calculated for each of these new models $[v_{\text{model}}(f)]$ and for the starting model $[v_0(f)]$. The corresponding relative velocity changes of the new models with respect to the starting model are then obtained by

$$\Delta_{\text{model}}(f) = \frac{v_{\text{model}}(f) - v_0(f)}{v_0(f)}. \tag{9}$$

The misfit μ to the observed velocity changes $\Delta_{\text{station}}(f)$ is then calculated by

$$\mu_{\text{model}} = \sqrt{\sum_{i=1}^{N}\left[\frac{\Delta_{\text{station}}(f_i) - \Delta_{\text{model}}(f_i)}{\sigma(f_i)}\right]^2 \Bigg/ \sum_{i=1}^{N}\left[\frac{1}{\sigma(f_i)}\right]^2}, \tag{10}$$

where N is either 4 or 5, depending on whether a coseismic velocity drop can be determined for the relevant station in the frequency range between 2.0 and 4.0 Hz. The model with the lowest misfit value is the one which explains the observed coseismic velocity drops the best. For the Iwate-Miyagi Nairiku earthquake, we performed the described depth modelling for the three stations with the largest coseismic velocity drops, that is, stations ICEH, ICWH and NRKH. The velocity drops at the different frequency ranges are shown in Fig. 10(b) with their respective standard deviations, where the CCs are used below 0.5 Hz and the SCs above. The stations exhibit three different behaviours from a rather linear increase of the velocity drop with frequency (ICEH) over a strong velocity drop increase (ICWH) to an almost constant velocity drop at the highest frequency ranges (NRKH). For station ICWH, the velocity drop could not be determined in the fifth frequency range. An overview of the results of the modellings (assumption 1 and 2) is shown in Fig. 10(c), the modellings according to assumption 1 in Figs 10(d)–(f).

In the modellings of assumption 1, there is a clear trade-off visible for stations ICEH and ICWH (Figs 10d and e). Models with a strong velocity change only at shallow layers or a smaller change reaching very deep give similar misfit values. For station ICEH, the minimum misfit (2.1×10^{-4}) is found for a velocity change of -0.25 per cent reaching 2.2 km deep. There is another local minimum (9.2×10^{-4}) for a coseismic velocity change of -4.25 per cent constrained to the shallowest 100 m. For station ICWH, the trade-off is even larger than for ICEH. The global misfit minimum is very low (6.1×10^{-5}) and corresponds to a velocity change of -1.3 per cent down to a depth of 800 m. However, there

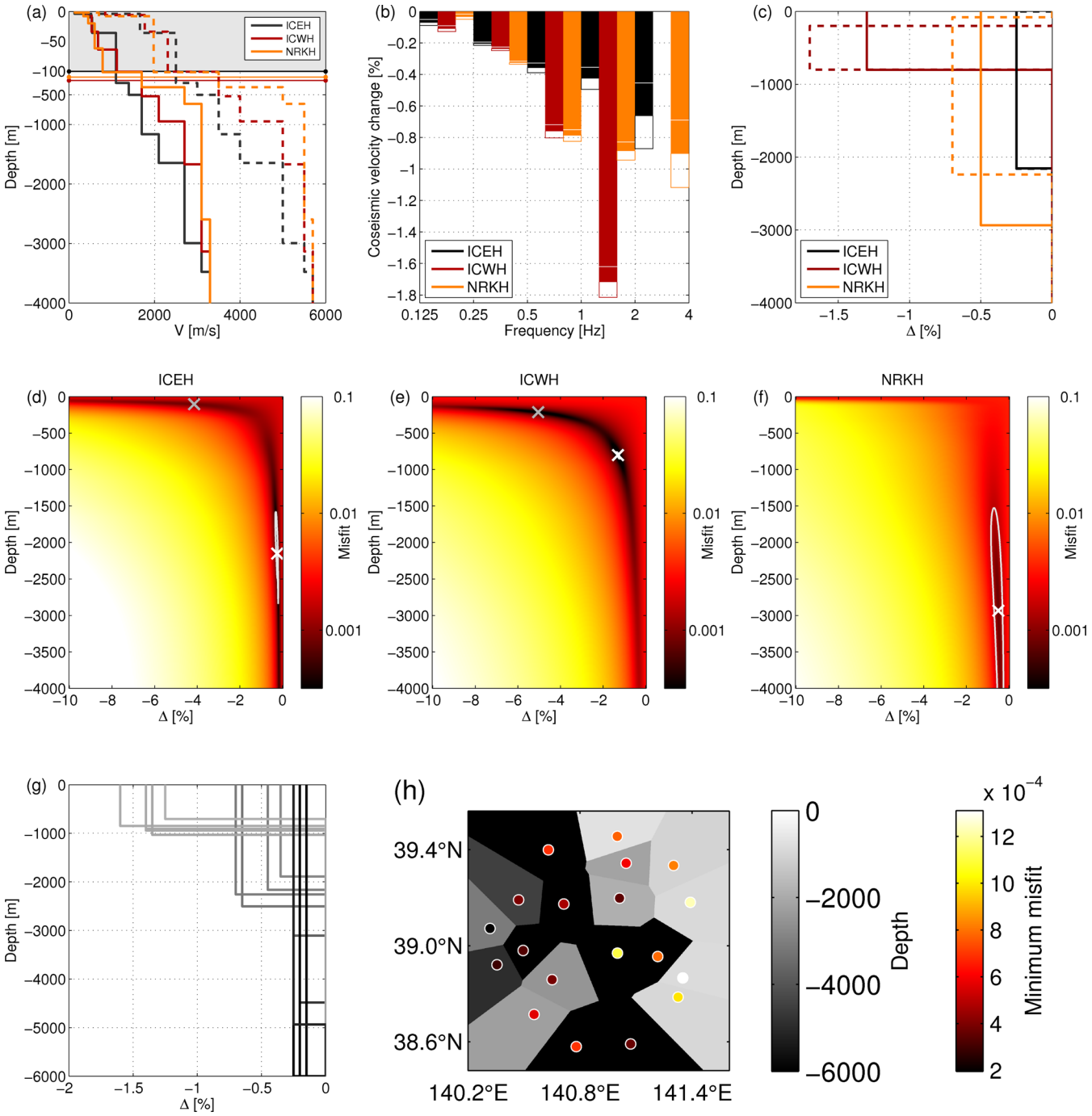

Figure 10. (a–f) Modelling the depth distribution of the coseismic velocity changes during the Iwate-Miyagi Nairiku earthquake for the three stations ICEH, ICWH and NRKH: (a) Reference shear- (solid lines) and pressure-wave (dashed lines) velocity profiles. Above the Hi-net borehole depth (indicated by the horizontal lines), the velocity profiles correspond to the borehole logs. Below, they correspond to the J-SHIS velocity structure. Note the different scale for the upper 100 m (grey background). (b) Velocity drops during the Iwate-Miyagi Nairiku earthquake in different frequency ranges. Below 0.5 Hz, the data are obtained by CC analysis, above 0.5 Hz by SC analysis. The white/coloured lines indicate the error bars. For ICWH, no velocity drop can be determined between 2.0 and 4.0 Hz. (c) Results of the depth modelling for the three stations. Only the best-fitting models are shown. The modelling according to assumption 1, that is, a constant relative velocity drop between the surface and a certain depth, is shown as a solid line, the modelling for assumption 2 with a constant relative drop between two depths is shown as a dashed line. For ICEH, both assumptions yield the same result. (d–f) Results of the modelling for assumption 1, that is, the misfit as a function of depth and velocity drop. The best-fitting models are indicated by the white cross, the grey contour line corresponds to twice the minimum misfit. For ICEH and ICWH, a second local minimum is indicated by the grey cross. (g–h) Modelling of the coseismic velocity changes during the Tohoku earthquake for all stations running at that time using assumption 1: The velocity change profiles (g) for the different stations are shown in different shades of grey, according to the depth of the velocity changes. In the overview map(h), the background colour also corresponds to the depth of the velocity changes. The colour of the circles at the station locations corresponds to the minimum misfit value of the station's modellings.

is second minimum (2.4×10^{-4}) corresponding to a change of -5.0 per cent in the shallowest 210 m. For both sites, ICEH and ICWH, the strong trade-off makes it difficult to actually determine the depth range of the coseismic velocity changes. For the third site, NRKH, strong velocity changes in shallow layers are incompatible with the measurements. The modelling indicates that the velocity change must have occurred deeper than 1 km. The minimum misfit (7.3×10^{-4}) corresponds to a velocity change of -0.5 per cent down to 3.0 km. However, the misfit value is larger than for the other sites, indicating that the modelling is less reliable here.

In Fig. 10(c), the coseismic velocity changes at depth for the modelling of both assumptions are shown together. For the modelling of assumption 2, only the velocity changes for the minimum misfits are shown, their results are quite similar to the two-parameter results. As expected, the misfit values are smaller for assumption 2 as assumption 1 is included as a special case, but the minimum misfit differences are not so significant. For station ICEH, both assumptions actually give the same result. For station ICWH, the lower limit of the velocity change remains unchanged, but the velocity change only occurs at depths below 200 m and the velocity drop increases to -1.7 per cent for assumption 2. At station NRKH, the velocity drop for assumption 2 is located between 80 m and 2.2 km depth, with a relative change of -0.7 per cent.

Although the modelling here with four or five used frequency ranges is supposed to be more precise than with only three frequencies as in Hobiger *et al.* (2012), there is still a very clear trade-off between large shallow changes and small deep changes. Only for NRKH do the higher frequencies actually increase the resolution. Using the deconvolution between the surface and borehole seismometers, Takagi *et al.* (2012) found velocity drops of the order of 5 per cent for stations ICEH (borehole depth: 108 m) and ICWH (260 m), but no significant velocity drop for NRKH (203 m). For ICEH and ICWH, our modelling is in agreement with these findings if we take the strong trade-off into account [the secondary minima are actually very close to the results of Takagi *et al.* (2012)]. For station NRKH, the combinations of both analyses argues for a deeply located change of smaller size.

For the 2011 Tohoku earthquake, we performed only the modelling of assumption 1 for all stations. The results are shown in Figs 10(g) and (h). The grey background colours in the map (h) indicate the depth of the respective velocity changes and are the same as the colours of the curves in (g). The colour of the dots, which mark the station sites, indicate the misfit values of the modelling for the respective stations. For stations in the east, the best-fitting results correspond to larger velocity drops of the order of -1.4 per cent at depths down to 1 km. However, the modelling for these stations is worse than for the other stations, as indicated by the systematically larger minimum misfit values. The observations at all other sites are best explained with smaller, but deeper velocity changes. The observations at two stations in the southwest (NRKH and MGMH) are best explained by velocity changes of about -0.7 per cent down to about 2.5 km. Two other stations in the north (HMSH and KGSH) are best modelled by velocity changes of about -0.4 per cent down to about 2 km. All other stations are best explained with velocity drops of less than -0.25 per cent, but reaching to more than 3 km in depth. Although the clustering of the different behaviours is evident, it is not easy to interpret these findings. A comparison with the peak ground acceleration (PGA) values of the Tohoku earthquake (Fig. 12) only gives some indications. The stations in the east which are best explained by larger shallow velocity changes are among the stations with the largest PGA values during the earthquake. However, other stations in the centre with similar PGA values have completely different modelling results. In the west, were the coseismic PGA values were low, the coseismic velocity changes were small, but deep.

6 DISCUSSION

6.1 Comparison of the SC, AC and CC performances

The principal advantages of the different correlation methods have already been discussed. One advantage of the CC analysis is the robustness which can be obtained by combining the 18 possible component combinations. The SC analysis only has six independent component combinations, the AC three. For SC and CC, the signals can be whitened spectrally before the actual correlations, setting the energy contribution of each frequency to the same value. This treatment is unfortunately not possible with ACs. Therefore, they are more vulnerable if single frequencies, for example, anthropogenic noise, dominate the signals. Furthermore, the stretching of the signals used to detect velocity changes corresponds to a variation of the frequency range. In the case of predominant frequencies, this can pose a serious problem. A main problem of the CC technique is its failure for large station distances at high frequencies. Therefore, going to higher frequencies would require a closer station spacing. For the AC and SC techniques, based on single sensors, this frequency problem does not exist and higher frequencies can thus be attained.

Another disadvantage of the CC technique is the actual location of the velocity changes. As only velocity changes for pairs of stations are measured, tomography algorithms which are based on assumptions on the scattering regime have to be used (Barmin *et al.* 2001; Brenguier *et al.* 2007; Hobiger *et al.* 2012). Using the AC and SC techniques, the velocity changes determined for the single stations can be regarded as a good approximation for the actual velocity changes at the exact station location and no tomography algorithm is necessary to get a good impression of the spatial velocity change distribution.

As we analysed the same data with the three different correlation techniques, we can investigate how the properties of the different techniques really affect the results. We use the fit parameter χ as a quality indicator for the velocity variation curves. Although χ depends on whether the fit model is appropriate for the data or not, it does not penalize data with lower correlation coefficients when using the definition of eq. (7). Indeed, the correlation coefficients of the different data points influence χ, but χ is mainly sensitive to how good the data actually match the used model. The model we used for the fit includes coseismic velocity drops and post-seismic recovery for both earthquakes and seasonal variations with a period of one year. Any other effects, for example, short-scale variations caused by earth tides, are not included in the model. If such effects occur, the fit will get worse. The large majority of the velocity variation curves are very well described by the fit model of eq. (5), for example, those curves shown in Fig. 5. In Fig. 11, the χ values of the different stations or station pairs are compared for the different correlation techniques and in different frequency ranges. The orange dashed line ($\chi = 0.11$) marks the empirical limit under which the data are well fitted. This limit was used in the previous sections to determine the good stations. The percentage at the top of the figures indicates the ratio of stations for which the data are actually well fitted. In the lowest frequency range below 0.25 Hz, the fit is much better for CC than for SC and AC, for which only slightly more than half of the stations have good data fits. In all

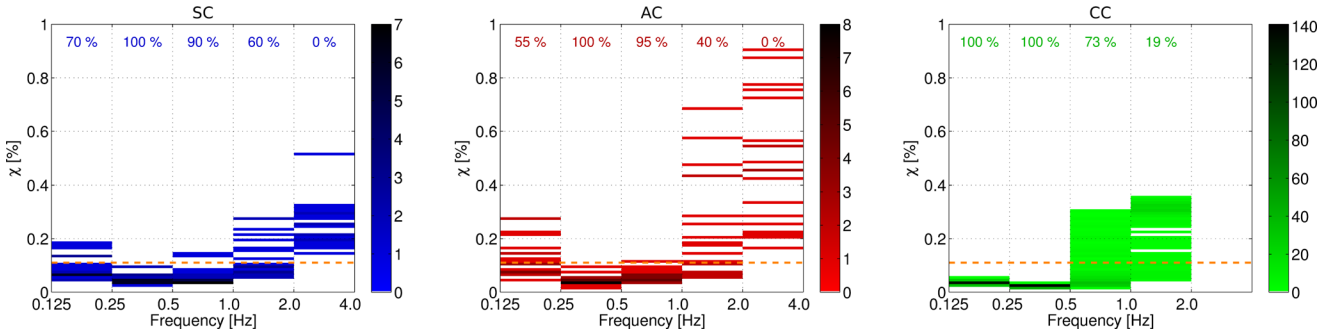

Figure 11. Statistics on the fit quality for the different stations or station pairs of the different correlation techniques. The χ values for fitting the velocity variation curves of the different stations or station pairs with eq. (5) are shown. The figure indicates how many stations or station pairs exhibit the respective χ values (rounded with a precision of 0.1 per cent). For SC and AC, there are 20 stations in total. For CC, there are 190 station pairs.

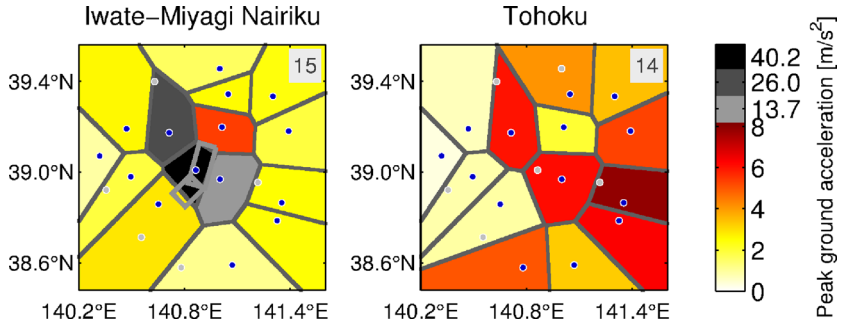

Figure 12. Peak ground accelerations of the KiK-net stations which are located at the surface of the Hi-net boreholes for the 2008 Iwate-Miyagi Nairiku and the 2011 Tohoku earthquakes. Only stations which were operational at the time of the respective earthquakes are shown. Their number is indicated in the upper right corner of the respective figures.

techniques, the best fits occur in the frequency range between 0.25 and 0.5 Hz. Here again, the CC curves are fitted best, but all SC and AC curves also have good χ values. Between 0.5 and 1.0 Hz, the SC and AC curves are still well fitted, but the CCs start to degrade with only 73 per cent of good station pairs. Between 1.0 and 2.0 Hz, all correlation techniques degrade, but the best results are still achieved with the SC which has more than half of the stations with good fits. The AC fits are worse here and actually show some stations with very bad fits. About one fifth of the CC station pairs still yields a good fit. In the highest frequency range above 2.0 Hz, there is not a single station with a good fit in SC and AC, but overall, the SC fits are still better than the AC fits.

To conclude, we can state that the best results are found with CC at frequencies below 0.5 Hz and with SC for frequencies above 0.5 Hz. The CC analysis is usually reliable up to frequencies of 1.0 Hz and for some station pairs even up to 2.0 Hz. The SC and AC analyses extend our knowledge of the velocity changes to higher frequencies, where the SC gives more reliable results than the AC.

6.2 Relation between coseismic velocity changes and PGAs

Coseismic velocity changes are visible for both the Iwate-Miyagi Nairiku and the Tohoku earthquake. A result of the CC analysis (Hobiger *et al.* 2012) was that the coseismic velocity changes occurring at the Iwate-Miyagi Nairiku earthquake are correlated with the PGA caused by the earthquake with the exception of station NRKH which shows a strong coseismic velocity drop, but did not experience a major acceleration during the earthquake shaking. We will examine the PGA effect on the coseismic velocity drops for the SC results of both earthquakes. The Hi-net boreholes are equipped with accelerometers of the KiK-net network at surface and depth. Most of these stations were operational during both earthquakes. The three-component PGAs of the surface sensors are shown in Fig. 12 for both earthquakes. During the Iwate-Miyagi Nairiku earthquake, station ICWH, located just above the epicentre, recorded a PGA of over 4*g*. Other stations in the surroundings of the fault zone also recorded accelerations greater than gravity. At the location of station NRKH in the southwest of the fault zone, where the largest coseismic velocity changes were observed, the recorded PGA was only about 0.3*g*. During the Tohoku earthquake, all stations measured accelerations below gravity and there is a systematic decrease in acceleration from east to west.

The coseismic velocity changes in three frequency ranges are shown in relation with the measured PGAs in Fig. 13(a) for the Iwate-Miyagi Nairiku earthquake. As the velocity changes below 0.25 Hz were small, only the three higher frequency ranges between 0.25 and 2.0 Hz are shown. In all three frequency ranges, there is a clear increase of the coseismic velocity drop with PGA with the exception of station NRKH (the green symbols in the figure), which exhibited the largest coseismic velocity changes below 1.0 Hz, but encountered a moderate PGA. Station ICWH suffered the largest PGA during the shaking and showed the largest coseismic velocity changes above 1.0 Hz. The dashed lines in the figure are obtained by a linear fit to all data points except the NRKH data. As a result of the logarithmic scale of the PGA axis, the linear fit lines are curved. These lines also show the clear trend of increasing velocity drop with PGA, which is strongest for frequencies between 0.5 and 2.0 Hz. However, the points are still quite scattered around the trend. As we were able to separate recovering and non-recovering velocity

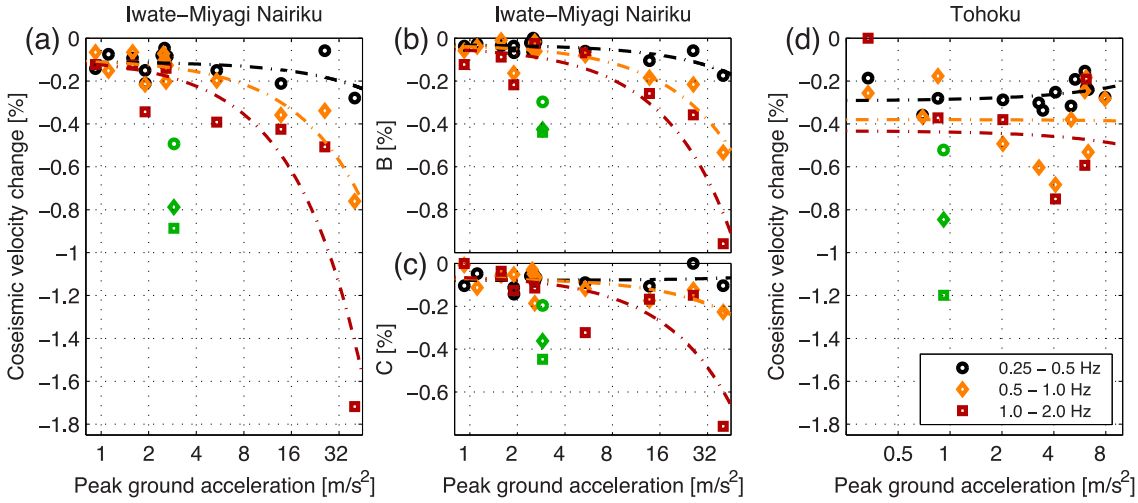

Figure 13. Comparison of the three-component peak ground accelerations measured by the KiK-net accelerometers at the surface of the Hi-net boreholes with the SC coseismic velocity changes for the Iwate-Miyagi Nairiku earthquake (left) and the Tohoku earthquake (right) in different frequency ranges. For the Iwate-Miyagi Nairiku earthquake, the coseismic velocity changes can also be separated in non-recovering velocity changes (parameter *B*; centre top) and recovering changes (parameter *C*; centre bottom). The dashed curves are linear fits to the data of the respective frequency ranges, neglecting the data of station NRKH (shown in green). Due to the logarithmic scale of the abscissa, the lines are curved.

changes by the curve fitting with eq. (5), we can also search for differences in both behaviours caused by the strong shaking effect. The respective results are shown in Figs 13(b) and (c). The non-recovering velocity drops (parameter *B* in eq. 5), show a stronger velocity drop increase with PGA than the recovering velocity drops (parameter *C* in eq. 5). The latter is almost flat between 0.25 and 0.5 Hz and its velocity drop increase is lower than 70 per cent of the increase of the non-recovering drops. The recovering and non-recovering velocity drops of station NRKH are of similar size and do not fit well with the changes of the other stations. For station ICWH, the recovering and non-recovering changes are also of similar size, but they are, at least between 1.0 and 2.0 Hz, larger than expected from the trend fits of the other stations.

For the Tohoku earthquake, the maximum PGA in the study region was much smaller than for the first earthquake, but a larger area was affected by strong shaking. The data in Fig. 13(d) do not show a clear trend. The fitted trend lines are actually rather flat, so that stations with moderate PGA have coseismic velocity drops comparable to other stations with much larger PGA, but there is still a lot of scattering around the trend lines. An exception here is also station NRKH which shows much larger velocity changes than all the other stations in all frequency ranges.

Nonlinear subsurface effects caused by strong ground shaking are a possible explanation for our results. They are a good explanation for the non-recovering effects of the Iwate-Miyagi earthquake and can also explain parts of the recovering effects, where non-recovering effects are effects which recover on a much longer timescale than the analysed 3.5 yr. For the Tohoku earthquake, nonlinear effects by strong shaking cannot explain the observed velocity changes. Furthermore, station NRKH experienced only moderate shaking during both earthquakes, but the strongest coseismic velocity changes. Other processes have to be taken into account to explain all of the coseismic velocity changes.

The particularity of the observations at station NRKH might be caused by the location of this station in Onikobe Caldera (Nakajima & Hasegawa 2003), which is a region famous for its hot spas. Therefore, the shallow crust beneath station NRKH is different to the other stations.

6.3 Interpretation of the depth of the coseismic velocity changes

After having performed the depth modelling of the coseismic velocity changes in Section 5, our final interpretation for the Iwate-Miyagi Nairiku earthquake is that most of the observed coseismic velocity changes are actually caused by nonlinear effects due to strong ground shaking during the earthquake. In the literature, such effects have been proposed by many authors (e.g. Li *et al.* 1998; Rubinstein & Beroza 2004, 2005; Schaff & Beroza 2004; Li *et al.* 2006; Peng & Ben-Zion 2006; Rubinstein *et al.* 2007). The largest velocity changes around the fault zone are mostly non-recovering during the observation time. Coseismic velocity changes further away from the fault zone recover to a larger degree during the observation time. These recovering changes are less related to strong ground shaking, but difficult to explain. A possible explanation might be the change of static stress, strain or strain rate caused by the earthquake (e.g. Poupinet *et al.* 1984; Rivet *et al.* 2011). According to this explanation, regions of decreasing stress should also exhibit decreases in seismic velocity and the recovery times should be large. However, we neither see coseismic increases in seismic velocity (as should be the case in areas of increasing stress) nor large recovery times for the recovering changes. Further possible explanations of the recovering changes are water-level changes (Sens-Schönfelder & Wegler 2006) or pore-pressure changes (Schaff & Beroza 2004) caused by the earthquake. Such effects are supposed to recover on the order of a year, but velocity increases should also be observed. For station NRKH, the modelling indicates that the velocity changes lie deeper than for the other sites. The small coseismic PGA value of this site also suggests that strong ground shaking is not likely to be the cause of the observations. The location of the station in the southwestern part of the fault zone might play a role there. If we extend the fault model of Ohta *et al.* (2008) to the southwest, the depth of the rupture zone below station NRKH is about 4 km, similar to the depth down to which the velocity change of our modelling is located (Fig. 10). Coseismic velocity changes concentrated in the fault zone have already been discussed in Rubinstein *et al.* (2007).

For the Tohoku earthquake, it is very difficult to find a comprehensive explanation of the velocity changes. Strong ground shaking

caused by the earthquake does not have an effect on the amplitude of the observed velocity changes and can therefore not explain them. Thus, possible explanations might be the large-scale effect of seismic stress changes by the Tohoku earthquake or water-level changes in the area. It can be speculated that the larger velocity changes experienced by station NRKH during the Tohoku earthquake compared with the other stations might be due to a reactivation of the damages of the Iwate-Miyagi Nairiku earthquake, which had partly recovered between both earthquakes.

Anyhow, the Tohoku earthquake affected a much larger area than covered by this study. A systematic study of the coseismic effects in the complete northeastern part of Honshu may prove more successful in giving a comprehensive explanation of the observed velocity changes.

6.4 Possible causes of the seasonal velocity variations

We found seasonal velocity variations using all three correlation techniques. These seasonal variations are well described by a cosine function with a period of 1 yr. At frequencies below 0.5 Hz, different stations show very different seasonal effects, not only in amplitude, but especially in phase, that is, the different stations show the velocity maximum at completely different times of the year. For higher frequencies, the phases of the different stations are in good agreement and are very similar for both frequency ranges between 0.5 and 1.0 Hz and between 1.0 and 2.0 Hz. In both frequency ranges, the velocity maximum occurs in the last third of October. The amplitudes of these effects, however, vary a lot for the different stations.

Possible reasons for the seasonal variations have been discussed in Hobiger *et al.* (2012). The effects at low frequencies might be caused by seasonal changes of the main seismic noise sources. At these frequencies, the seismic noise is mainly produced in the oceans (Longuet-Higgins 1950), but the actual source regions change during the year (Stehly *et al.* 2006). Zhan *et al.* (2013) showed that a seasonal variation of the seismic noise spectrum may be the cause for the observation of seasonal variations when measured by the stretching technique. We cannot exclude that such effects actually cause our observations at low frequencies. At higher frequencies, the main noise sources are anthropogenic. For these frequencies, the observations of the different stations or station pairs are in better agreement among one another. Possible causes for the seasonal variations at these frequencies may be water-level changes due to seasonal precipitation variations (Sens-Schönfelder & Wegler 2006) or thermoelastically induced strain variations in the shallow subsurface layers as proposed by Meier *et al.* (2010). In any case, GPS measurements also showed seasonal variations of the eastward plate motion in northeastern Japan, which is faster during the winter (Murakami & Miyazaki 2001). Heki (2001) found seasonal variations on the vertical components of GPS measurements and explained them by a seasonal variation of the strain buildup in northeastern Japan due to snow loads. The snow depths in the area are at a maximum in March and melting occurs in spring and early summer, at the time of the year where the seismic wave velocity is at a minimum.

7 CONCLUSION

In this paper, we introduced the SC technique which consists of calculating the correlations between different components of the same three-component seismometer. The usable frequency range of this technique is higher than that of CCs, which are limited by the distance between the sensors of each station pair. The main advantage of the SC technique with respect to ACs is the possibility of spectral whitening of the signals, and therefore the greater robustness in the case of seismic noise with predominant frequencies, for example, caused by anthropogenic sources. In this study, the CC technique turned out to be the most reliable technique for frequencies below 0.5 Hz. Above that frequency, the SC technique proved to be the most reliable technique.

For both analysed earthquakes we found a systematic increase of the coseismic velocity changes with frequency. For the Iwate-Miyagi Nairiku earthquake, the largest coseismic velocity changes occurred close to the fault zone, with a maximum in its southern part. The measurements show that more than half of the coseismic velocity changes do not recover significantly over the analysis period. The rest of the coseismic velocity changes recover on a timescale of the order of half a year. For the Tohoku earthquake, all of the study area is affected by significant coseismic velocity changes.

We tried to model the depth range of the coseismic velocity changes. For the Iwate-Miyagi Nairiku earthquake, we found two stations where small, but deep velocity changes explain the observations in a similar way as large, but shallow velocity changes. For a third station, we found a clear indication for a deeper velocity change. For the Tohoku earthquake, there were clusters of stations for which the observations can be explained in different ways. For stations in the east, the best explanation were larger velocity changes reaching less than 1 km deep. For the other stations, deeper effects are more likely to explain the observed velocity changes. Nevertheless, further research in other areas affected by the Tohoku earthquake is necessary to get a comprehensive overview of the earthquake's effects.

Seasonal velocity variations have been observed with consistent phases for frequencies above 0.5 Hz. The maximum of these seasonal variations occurs in the end of October. The actual reasons for these observations are unclear, but possible explanations include seasonal variations in water level caused by precipitation changes, seasonal variations of the strain in the crust or variations caused by snow loading and melting.

Future work will consist of a qualitative and quantitative comparison of velocity change observations for other earthquakes in Japan and will show if the effects described in this analysis are general features of crustal earthquakes.

ACKNOWLEDGEMENTS

This work is funded by the German Research Foundation (DFG) and the Japan Society for the Promotion of Science (JSPS). The integrated event catalogue was compiled by the Japan Meteorological Agency and the Ministry of Education, Culture, Sports, Science and Technology in Japan. The data of the three surface stations were provided by the Japan Meteorological Agency. Dispersion curves were calculated with the geopsy code (available at http://www.geopsy.org). ASTER GDEM is a product of METI and NASA. We would like to thank the editor and two anonymous reviewers for their precious comments and help with improving this paper.

REFERENCES

Aoi, S., Kunugi, T. & Fujiwara, H., 2008. Trampoline effect in extreme ground motion, *Science,* **322,** 727–730.

Barmin, M.P., Ritzwoller, M.H. & Levshin, A.L., 2001. A fast and reliable method for surface wave tomography, *Pure appl. geophys.,* **158,** 1351–1375.

Bensen, G.D., Ritzwoller, M.H., Barmin, M.P., Levshin, A.L., Lin, F., Moschetti, M.P., Shapiro, N.M. & Yang, Y., 2007. Processing seismic ambient noise data to obtain reliable broad-band surface wave dispersion measurements, *Geophys. J. Int.,* **169,** 1239–1260.

Brenguier, F., Shapiro, N.M., Campillo, M., Nercessian, A. & Ferrazzini, V., 2007. 3-D surface wave tomography of the Piton de la Fournaise volcano using seismic noise correlations, *Geophys. Res. Lett.,* **34,** L02305, doi:10.1029/2006GL028586.

Brenguier, F., Campillo, M., Hadziioannou, C., Shapiro, N.M., Nadeau, R.M. & Larose, E., 2008a. Postseismic relaxation along the San Andreas fault at Parkfield from continuous seismological observations, *Science,* **321,** 1478–1481.

Brenguier, F., Shapiro, N.M., Campillo, M., Ferrazzini, V., Duputel, Z., Coutant, O. & Nercessian, A., 2008b. Towards forecasting volcanic eruptions using seismic noise, *Nat. Geosci.,* **1,** 126–130.

Campillo, M. & Paul, A., 2003. Long-range correlations in the diffuse seismic coda, *Science,* **299,** 547–549.

Chen, J.H., Froment, B., Liu, Q.Y. & Campillo, M., 2010. Distribution of seismic wave speed changes associated with the 12 May 2008 Mw 7.9 Wenchuan earthquake, *Geophys. Res. Lett.,* **37,** L18302, doi:10.1029/2010GL044582.

Durand, S., Montagner, J.P., Roux, P., Brenguier, F., Nadeau, R.M. & Ricard, Y., 2011. Passive monitoring of anisotropy change associated with the Parkfield 2004 earthquake, *Geophys. Res. Lett.,* **38,** L13303, doi:10.1029/2011GL047875.

Fujiwara, H. *et al.*, 2009. A study on subsurface structure model for deep sedimentary layers of Japan for strong-motion evaluation, Tech. Note 337, National Research Institute for Earth Science and Disaster Prevention, Tsukuba, Japan, in Japanese.

Heki, K., 2001. Seasonal modulation of interseismic strain buildup in northeastern Japan driven by snow loads, *Science,* **293,** 89–92.

Hirose, F., Miyaoka, K., Hayashimoto, N., Yamazaki, T. & Nakamura, M., 2011. Outline of the 2011 off the Pacific coast of Tohoku Earthquake (M_W 9.0)—seismicity: foreshocks, mainshock, aftershocks, and induced activity, *Earth Planets Space,* **63,** 513–518.

Hobiger, M., Wegler, U., Shiomi, K. & Nakahara, H., 2012. Coseismic and postseismic elastic wave velocity variations caused by the 2008 Iwate-Miyagi Nairiku earthquake, Japan, *J. geophys. Res.,* **117,** L14303, doi:10.1029/2012JB009402.

Kubo, H. & Kakehi, Y., 2013. Source process of the 2011 Tohoku Earthquake estimated from the joint inversion of teleseismic body waves and geodetic data including seafloor observation data: Source model with enhanced reliability by using objectively determined inversion settings, *Bull. seism. Soc. Am.,* **103,** 1195–1220.

Larose, E. *et al.*, 2006. Correlation of random wavefields: an interdisciplinary review, *Geophysics,* **71,** SI11–SI21.

Li, Y.-G., Vidale, J.E., Aki, K., Xu, F. & Burdette, T., 1998. Evidence of shallow fault zone strengthening after the 1992 M7.5 Landers, California, earthquake, *Science,* **279,** 217–219.

Li, Y.-G., Vidale, J.E., Day, S.M., Oglesby, D.D. & Cochran, E., 2003. Postseismic fault healing on the rupture zone of the 1999 M7.1 Hector Mine, California, earthquake, *Bull. seism. Soc. Am.,* **93,** 854–869.

Li, Y.-G., Chen, P., Cochran, E.S., Vidale, J.E. & Burdette, T., 2006. Seismic evidence for rock damage and healing on the San Andreas fault associated with the 2004 M6.0 Parkfield earthquake, *Bull. seism. Soc. Am.,* **96,** S349–S363.

Lobkis, O.I. & Weaver, R.L., 2001. On the emergence of the Green's function in the correlations of a diffuse field, *J. acoust. Soc. Am.,* **110,** 3011–3017.

Longuet-Higgins, M.S., 1950. A theory of the origin of microseisms, *Phil. Trans. R. Soc. Lond. A,* **243,** 1–35.

Maeda, T., Obara, K. & Yukutake, Y., 2010. Seismic velocity decrease and recovery related to earthquake swarms in a geothermal area, *Earth Planets Space,* **62,** 685–691.

Maeda, T., Furumura, T., Sakai, S. & Shinohara, M., 2011. Significant tsunami observed at ocean-bottom pressure gauges during the 2011 off the Pacific coast of Tohoku Earthquake, *Earth Planets Space,* **63,** 803–808.

Meier, U., Shapiro, N.M. & Brenguier, F., 2010. Detecting seasonal variations in seismic velocities within Los Angeles basin from correlations of ambient seismic noise, *Geophys. J. Int.,* **181,** 985–996.

Murakami, M. & Miyazaki, S., 2001. Periodicity of strain accumulation detected by permanent GPS array: possible relationship to seasonality of major earthquakes' occurence, *Geophys. Res. Lett.,* **28,** 2983–2986.

Nakajima, J. & Hasegawa, A., 2003. Tomographic imaging of seismic velocity structure in and around the Onikobe volcanic area, northeastern Japan: implications for fluid distribution, *J. Volc. Geotherm. Res.,* **127,** 1–18.

Nakata, N. & Snieder, R., 2012. Estimating near-surface shear wave velocities in Japan by applying seismic interferometry to KiK-net data, *J. geophys. Res.,* **117,** B01308, doi:10.1029/ 2011JB008595.

NIED F-net, 2008. Available at: http://www.fnet.bosai.go.jp/event/tdmt.php?LANG=en&ID=20080613234200 (last accessed July 11, 2013).

Nishimura, T. *et al.*, 2005. Temporal changes in seismic velocity of the crust around Iwate volcano, Japan, as inferred from analyses of repeated active seismic experiment data from 1998 to 2003, *Earth Planets Space,* **57,** 491–505.

Niu, F., Silver, P.G., Daley, T.M., Cheng, X. & Majer, E.L., 2008. Preseismic velocity changes observed from active source monitoring at the Parkfield SAFOD drill site, *Nature,* **454,** 204–208.

Ohmi, S., Hirahara, K., Wada, H. & Ito, K., 2008. Temporal variations of crustal structure in the source region of the 2007 Noto Hanto Earthquake, central Japan, with passive image interferometry, *Earth Planets Space,* **60,** 1069–1074.

Ohta, Y. *et al.*, 2008. Coseismic fault model of the 2008 Iwate-Miyagi Nairiku earthquake deduced by a dense GPS network, *Earth Planets Space,* **60,** 1197–1201.

Okada, T. *et al.*, 2011. Shallow inland earthquakes in NE Japan possibly triggered by the 2011 off the Pacific coast of Tohoku Earthquake, *Earth Planets Space,* **63,** 749–754.

Okada, Y., Kasahara, K., Hori, S., Obara, K., Sekiguchi, S., Fujiwara, H. & Yamamoto, A., 2004. Recent progress of seismic observation networks in Japan—Hi-net, F-net, K-NET and KiK-net, *Earth Planets Space,* **56,** xv–xxviii.

Pacheco, C. & Snieder, R., 2005. Time-lapse travel time change of multiply scattered acoustic waves, *J. acoust. Soc. Am.,* **118,** 1300–1310.

Pacheco, C. & Snieder, R., 2006. Time-lapse traveltime change of singly scattered acoustic waves, *Geophys. J. Int.,* **165,** 485–500.

Paul, A., Campillo, M., Margerin, L. & Larose, E., 2005. Empirical synthesis of time-asymmetrical green functions from the correlation of coda waves, *J. geophys. Res.,* **110,** doi:10.1029/2004JB003521.

Peng, Z. & Ben-Zion, Y., 2006. Temporal changes of shallow seismic velocity around the Karadere-Düzce branch of the North Anatolian Fault and strong ground motion, *Pure appl. geophys.,* **163,** 567–600.

Poupinet, G., Ellsworth, W.L. & Fréchet, J., 1984. Monitoring velocity variations in the crust using earthquake doublets: an application to the Calaveras fault, California, *J. geophys. Res.,* **89,** 5719–5731.

Rivet, D., Campillo, M., Shapiro, N.M., Cruz-Atienza, V., Radiguet, M., Cotte, N. & Kostoglodov, V., 2011. Seismic evidence of nonlinear crustal deformation during a large slow slip event in Mexico, *Geophys. Res. Lett.,* **38,** L08308, doi:10.1029/2011GL047151.

Rubinstein, J.L. & Beroza, G.C., 2004. Evidence of widespread nonlinear strong ground motion in the M_W 6.9 Loma Prieta earthquake, *Bull. seism. Soc. Am.,* **94,** 1595–1608.

Rubinstein, J.L. & Beroza, G.C., 2005. Depth constraints on nonlinear strong ground motion from the 2004 Parkfield earthquake, *Geophys. Res. Lett.,* **32,** L14313, doi:10.1029/2005GL023189.

Rubinstein, J.L., Uchida, N. & Beroza, G.C., 2007. Seismic velocity reductions caused by the 2003 Tokachi-Oki earthquake, *J. geophys. Res.,* **112,** B05315, doi:10.1029/2006JB004440.

Sawazaki, K., Sato, H., Nakahara, H. & Nishimura, T., 2009. Time-lapse changes of seismic velocity in the shallow ground caused by stong ground motion shock of the 2000 Western-Tottori Earthquake, Japan, as revealed from coda deconvolution analysis, *Bull. seism. Soc. Am.,* **99,** 352–366.

Schaff, D.P. & Beroza, G.C., 2004. Coseismic and postseismic velocity changes measured by repeating earthquakes, *J. geophys. Res.,* **109,** B10302.

Sens-Schönfelder, C. & Wegler, U., 2006. Passive image interferometry and seasonal variations of seismic velocities at Merapi Volcano, Indonesia, *Geophys. Res. Lett.,* **33,** L21302, doi:10.1029/2006GL027797.

Sens-Schönfelder, C. & Wegler, U., 2011. Passive image interferometry for monitoring crustal changes with ambient seismic noise, *Compt. Rend. Geosci.,* **343,** 639–651.

Shapiro, N.M. & Campillo, M., 2004. Emergence of broadband Rayleigh waves from correlations of the ambient seismic noise, *Geophys. Res. Lett.,* **31,** L07614, doi:10.1029/2004GL019491.

Shapiro, N.M., Campillo, M., Stehly, L. & Ritzwoller, M.H., 2005. High-resolution surface-wave tomography from ambient seismic noise, *Science,* **307,** 1615–1618.

Snieder, R., Grêt, A., Douma, H. & Scales, J., 2002. Coda wave interferometry for estimating nonlinear behavior in seismic velocity, *Science,* **295,** 2253–2255.

Stehly, L., Campillo, M. & Shapiro, N.M., 2006. A study of the seismic noise from its long-range correlation properties, *J. geophys. Res.,* **111,** B10306, doi:10.1029/2005JB004237.

Suzuki, W., Aoi, S. & Sekiguchi, H., 2010. Rupture process of the 2008 Iwate-Miyagi Nairiku, Japan, earthquake derived from near-source strong-motion records, *Bull. seism. Soc. Am.,* **100,** 256–266.

Takada, Y., Kobayashi, T., Furuya, M. & Murakami, M., 2009. Coseismic displacement due to the 2008 Iwate-Miyagi Nairiku earthquake detected by ALOS/PALSAR: Preliminary results, *Earth Planets Space,* **61,** e9–e12.

Takagi, R., Okada, T., Nakahara, H., Umino, N. & Hasegawa, A., 2012. Coseismic velocity change in and around the focal region of the 2008 Iwate-Miyagi Nairiku earthquake, *J. geophys. Res.,* **117,** B06315, doi:10.1029/2012JB009252.

Tsutsumi, H., Sugito, N., Koshiya, S., Ishiyama, T., Imaizumi, T., Marushima, N. & Hirouchi, D., 2010. Surface rupture of the 2008 Iwate-Miyagi Nairiku earthquake observed at Oshu and Ichinoseki cities, Iwate prefecture, northeast Japan, *J. Geography,* **119,** 826–840.

Ueno, T., Saito, T., Shiomi, K., Enescu, B., Hirose, H. & Obara, K., 2012. Fractional seismic velocity change related to magma intrusions during earthquake swarms in the eastern Izu peninsula, central Japan, *J. geophys. Res.,* **117,** B12305, doi:10.1029/2012JB009580.

Wapenaar, K., Draganov, D., Snieder, R., Campman, X. & Verdel, A., 2010a. Tutorial on seismic interferometry. Part 1—basic principles and applications, *Geophysics,* **75,** 75A 195–75A 209.

Wapenaar, K., Slob, E., Snieder, R. & Curtis, A., 2010b. Tutorial on seismic interferometry. Part 2—underlying theory and new advances, *Geophysics,* **75,** 75A211–75A227.

Wartman, J., Dunham, L., Tiwari, B. & Pradel, D., 2011. Landslides in eastern Honshu induced by the 2011 Tohoku earthquake, *Bull. seism. Soc. Am.,* **103,** 1503–1521.

Wegler, U. & Sens-Schönfelder, C., 2007. Fault zone monitoring with passive image interferometry, *Geophys. J. Int.,* **168,** 1029–1033.

Wegler, U., Nakahara, H., Sens-Schönfelder, C., Korn, M. & Shiomi, K., 2009. Sudden drop of seismic velocity after the 2004 M_W 6.6 mid-Niigata earthquake, japan, observed with passive image interferometry, *J. geophys. Res.,* **114,** B06305, doi:10.1029/2008JB005869.

Yamada, M., Mori, J. & Ohmi, S., 2010. Temporal changes of subsurface velocities during strong shaking as seen from seismic interferometry, *J. geophys. Res.,* **115,** B03302, doi:10.1029/2009JB006567.

Zhan, Z., Tsai, V.C. & Clayton, R.W., 2013. Spurious velocity changes caused by temporal variations in ambient noise frequency content, *Geophys. J. Int.,* **194,** 1574–1581.

Zhao, P.-P. *et al.*, 2012. Crustal velocity changes associated with the Wenchuan *M*8.0 earthquake by auto-correlation function analysis of seismic ambient noise, *Chin. J. Geophys.,* **55,** 137–145 (in Chinese with English abstract).